THESIS FOR THE DEGREE OF DOCTOR OF PHILOSOPHY

INTEGRATED NARROW-LINEWIDTH OPTICAL COHERENT OSCILLATORS IN ULTRA-LOW LOSS SILICON NITRIDE

Yi Sun

CHALMERS

Photonics Laboratory
Department of Microtechnology and Nanoscience (MC2)
Chalmers University of Technology
Göteborg, Sweden, 2026

Integrated narrow-linewidth optical coherent oscillators in ultra-low loss silicon nitride
Yi Sun
©Yi Sun, 2026

ISBN 978-91-8103-354-0
Doktorsavhandlingar vid Chalmers tekniska högskola,
Ny serie nr 5811
ISSN 0346-718X

Photonics Laboratory
Department of Microtechnology and Nanoscience (MC2)
Chalmers University of Technology
SE-412 96 Göteborg
Sweden
Telephone: +46 (0)31–772 10 00

Front cover illustration: The schematic illustration of an integrated narrow-linewidth optical parametric oscillator with a long external cavity.

Printed by Chalmers Reproservice
Chalmers Tekniska Högskola
Göteborg, Sweden, 2026

Integrated narrow-linewidth optical coherent oscillators in ultra-low loss silicon nitrides

Yi Sun
Photonics Laboratory
Department of Microtechnology and Nanoscience (MC2) Chalmers University of Technology

Abstract

In recent years, advancements in technologies such as optical coherent communication and precision measurement, have raised the bar for the coherence, power, noise, and other key parameters of light sources. On-chip light sources have emerged as the ideal solution when small size, low weight, low power consumption and cost-effectiveness matter the most. Currently, integrated light sources include semiconductor lasers and chip-based optical parametric oscillators. However, due to their small cavity volume, both types suffer from high quantum noise, poor coherence compared to solid-state or gas lasers.

As a popular integrated photonic platform, silicon nitride has a significant potential for addressing these challenges since it has high nonlinearity, wide transparent window, and good compatibility with other materials. In our previous work, we have realized low-loss long waveguides and microring resonators. In this thesis, we further reduce the propagation loss of dispersion-engineered silicon nitride waveguides by smoothing the sidewall roughness. By periodically modulating the losses of microring resonators, we achieve an on-chip optical parametric oscillator with a record signal power of 215 mW. In addition, we build a hybrid integration stage and suppress the intrinsic linewidth of a semiconductor laser to 9 Hz using self-injection locking method. Finally, by implementing external feedback circuits for optical parametric oscillators, we suppress the intrinsic linewidth of the signal to below 1 Hz using an optical fiber loop, and to approximately 10 Hz using an integrated waveguide loop. These results pave the way for on-chip integration of high-power, narrow-linewidth lasers and optical parametric oscillators.

Keywords: integrated photonics, silicon nitride, low loss, frequency noise, semiconductor laser, optical parametric oscillator, narrow linewidth

Publications

This thesis is based on the work contained in the following papers:

[A] **Yi Sun**, Zhichao Ye, Raphaël Van Laer, Anders Larsson, and Victor Torres-Company, "Low-loss dispersion-engineered silicon nitride waveguides coated with a thin blanket layer", *Conference on Lasers and Electro-Optics*, San Jose, USA, paper JW3B.183, 2022.

[B] **Yi Sun**, Fuchuan Lei, Yan Gao, and Victor Torres-Company, "High-power on-chip hyperparametric oscillator", *Optics Letters*, vol. 50, no. 15, pp. 4798-4801, 2025.

[C] Fuchuan Lei, **Yi Sun**, Óskar B. Helgason, Zhichao Ye, Yan Gao, Magnus Karlsson, Peter A. Andrekson, and Victor Torres-Company, "Self-injection-locked optical parametric oscillator based on microcombs", *Optica*, vol. 11, no. 3, pp. 420-426, 2024.

[D] **Yi Sun**, Fuchuan Lei, Carlos E. Osornio-Martinez, Yan Gao, Dawson B. Bonneville, Meindert Dijkstra, Sonia M. García-Blanco, and Victor Torres-Company, "Chip-scale narrow-linewidth optical parametric oscillators", submitted, 2026.

Related publications and conference contributions by the author, not included in the thesis:

[E] **Yi Sun**, Fuchuan Lei, Yan Gao, and Victor Torres-Company, "High-power optical parametric oscillators in silicon nitride", *Conference on Lasers and Electro-Optics Europe (CLEO/Europe)*, CD-14.1, 2025.

[F] **Yi Sun**, Yan Gao, and Victor Torres-Company, "On-chip narrow-linewidth optical parametric oscillators", submitted to Conference on Lasers and Electro-Optics, 2026.

[G] Fuchuan Lei, **Yi Sun**, Óskar B. Helgason, Zhichao Ye, Yan Gao, Magnus Karlsson, Peter A. Andrekson, and Victor Torres-Company, "Narrow-linewidth and tunable parametric oscillator", *Conference on Lasers and Electro-Optics*, Charlotte, USA, paper STh3I.3, 2024.

[H] Yan Gao, **Yi Sun**, Israel Rebolledo-Salgado, Raphaël Van Laer, Victor Torres-Company, and Jochen Schröder, "Tightly-Confined and Long Z-Cut Lithium Niobate Waveguide with Ultralow-Loss", *Laser Photonics Review*, pp. e00042, 2025.

[I] Sara Persia, **Yi Sun**, Vaishali Adya, and Victor Torres-Company, "Intensity difference squeezing of high-power modes in strongly overcoupled silicon nitride microresonators", submitted to Conference on Lasers and Electro-Optics, 2026.

[J] Sara Persia, **Yi Sun**, Vaishali Adya, and Victor Torres-Company, "Intensity difference squeezing of high-power modes in a strongly overcoupled silicon nitride microresonator", submitted to Optics Letters, 2026.

Contents

Abstract **iii**

Publications **v**

Acknowledgement **ix**

Acronyms **xi**

1 Introduction **1**
1.1 Historical overview 1
1.2 This thesis 6

2 Frequency noise in optical coherent oscillators **9**
2.1 Frequency noise 9
2.1.1 Basics of frequency noise 10
2.1.2 Spectral line shape 12
2.2 Frequency noises of optical coherent oscillators 14
2.2.1 Frequency noise of semiconductor lasers 14
2.2.2 Frequency noise of optical parametric oscillators . 16
2.2.3 Thermorefractive noise of microresonators 20
2.3 Self-heterodyne method 23

3 Optical coherent oscillators with external cavities **27**
3.1 External-cavity-induced linewidth reduction 27
3.2 Long-waveguide-based external cavity 29
3.3 Microring-based external cavity 30

4 Self-injection locking technique **35**
4.1 Dynamics of self-injection locked lasers 35
4.1.1 Laser dynamics 36

4.1.2 Linewidth reduction 38
4.2 Experimental study on self-injection locked lasers 39
4.2.1 Experimental procedures 40
4.2.2 Experimental results 43

5 Ultra-low loss silicon nitride waveguides 47
5.1 Waveguide losses 47
5.2 Overview of process flow 51
5.2.1 Wafer preparation 51
5.2.2 Waveguide patterning 53
5.2.3 Post-processing 54
5.3 Considerations for manufacturing long waveguides 55

6 Future outlook 59

7 Summary of papers 61

Papers 85

Acknowledgement

First, I would like to express my sincere gratitude to my supervisor, Prof. Victor Torres-Company, for his selfless guidance, valuable advice, continuous support and encouragement throughout my research process. His rigorous academic attitude and profound insights have had a lasting and significant impact on my development as a researcher. I am also deeply grateful for his exceptional management skills, which created a well-organized and supportive research environment, allowing me to pursue my doctoral studies with focus and peace of mind within the group.

I am also grateful to my co-supervisor Prof. Bart Kuyken, Assoc. Prof. Raphaël Van Laer and examiner Prof. Åsa Haglund, for profound academic insights, meticulous advice. I am also thankful to Prof. Peter Andrekson, and Prof. Magnus Karlsson for sharing knowledge and insights.

I would like to express my special thanks to Prof. Fuchuan Lei for patiently teaching experimental techniques, which enabled me to successfully complete the relevant experimental work. His professional knowledge and experimental support played a key role in the smooth progress of my project. At the same time, I would like to thank Dr. Zhichao Ye, Dr. Marcello Girardi, Dr. Yan Gao for their guidance in manufacturing photonic devices. Their experience and technical support were of great help to my research.

I am grateful to Dr. Kaiyi Wu and Dr. Xiaomin Lyu for the discussions on soliton generation and self-injection locking experiments. I am thankful to Carmen Haide López Ortega, Sara Persia, Vijay Shekhawat, Tim Fuhrmann, Niklas Hammerschmidt, Mia Buchmayr, Dr. Yvan Klaver for creating a harmonious and orderly environment for everyone, allowing us to share research progresses, help each other, and grow together.

I would also like to thank Dr. Óskar B. Helgason, Dr. Israel Rebolledo-Salgado, Dr. Krishna Sundar Twayana, for their valuable contributions to the laboratory. Additionally, I would like to thank every member

of the Photonics Laboratory for their support and collaboration. My heartfelt thanks also go to the personnel responsible for maintaining equipment in the clean room, whose efforts are important to this work.

Finally, I would like to express my sincere gratitude to my parents and friends for their unconditional love and support, especially when I encountered difficulties and challenges. Their trust and support have always been my driving force to move forward.

Yi Sun
Göteborg, Sweden
February 2026

Abbreviations

LiDAR	light detection and ranging
DFB	distributed feedback
DBR	distributed Bragg reflector
CMOS	complementary metal–oxide–semiconductor
PIC	photonic integrated circuit
FP	Fabry–Pérot
FSR	free spectral range
RIN	relative intensity noise
SIL	self-injection locking
PSD	power spectral density
FWHM	full width at half-maximum
OPO	optical parametric oscillator
WDM	wavelength division multiplexer
VBG	volume Bragg grating
TRN	thermorefractive noise
AOM	acousto-optic modulator
PC	polarization controller
BPD	balanced photodetector
EDFA	erbium doped fiber amplifier
LPCVD	low-pressure chemical vapor deposition
SEM	scanning electron microscopy

Chapter 1

Introduction

1.1 Historical overview

The history of lasers began in 1917, when Einstein proposed the theory of stimulated emission [1]. After decades of development, Townes and colleagues were the first to construct a microwave amplification device, the maser, in 1953, experimentally verifying this principle [2]. In 1960, Maiman, building on the key design concepts of Schawlow and Townes [3], successfully developed the first ruby laser [4], marking the beginning of the era of practical lasers. Subsequently, many types of lasers, including the helium–neon laser [5] and the semiconductor laser [6], were developed. With its rapid development, laser technology has found widespread application in communications [7], industry [8], and scientific research [9], and now constitutes a cornerstone of modern science and technology.

Optical parametric oscillators (OPOs) represent another key class of coherent light sources, filling regions of the electromagnetic spectrum that conventional lasers cannot access due to the lack of suitable gain media [10]. Their fundamental principle is rooted in frequency conversion techniques in nonlinear optics, whereby second-order or third-order nonlinear effects efficiently convert a pump laser into signal and idler waves, enabling broadband coherent output spanning from the ultraviolet to the far-infrared [11–13]. As early as 1961, Franken used a ruby laser to demonstrate second-harmonic generation for the first time [14]. Decades of development have established the OPO as a key technology for filling spectral gaps inaccessible to conventional lasers. Owing to their unique features, such as wide tunability, high spectral purity, OPOs play

an irreplaceable role in a wide range of frontier fields, including spectroscopic analysis [15], quantum information [16], remote sensing [17] and biomedicine [18].

With continuous breakthroughs in key parameters of coherent light sources, such as wavelength coverage, output power, and optical linewidth, their applications have been expanding [19–23]. In particular, the rapid development in recent years of technologies including light detection and ranging (LiDAR) [24], optical clocks [25], coherent optical communications [26], and precision metrology [27] has imposed near-fundamental requirements on source coherence and frequency stability. Against this backdrop, narrow-linewidth light sources, owing to their superior spectral purity and low phase noise, have emerged as a central research focus [28–30]. To meet the growing demands for integration, miniaturization, and cost efficiency, the development of chip-scale narrow-linewidth light sources with high coherence and low noise has become a key challenge and an inevitable direction for enabling practical next-generation photonic integrated circuits and systems [31–34].

Narrow-linewidth semiconductor lasers

Semiconductor lasers are central to integrated photonics because they provide compact, electrically driven, and highly efficient chip-scale light sources which could be directly fabricated using mature semiconductor processing technologies. With the rapid growth in semiconductor laser applications, the scope of integrated optics has likewise broadened, driving further advancements within the field.

The earliest semiconductor lasers are based on Fabry–Pérot (FP) cavities [6], which have two reflectors and a single cavity, as shown in Fig. 1.1(a). The transverse mode of a laser is determined by the lateral size of the laser, while the longitudinal mode is determined by the laser cavity length. Usually, a short-cavity structure has a larger longitudinal mode spacing and can achieve single longitudinal mode operation without any assistance or mode selection, but due to the short photon lifetime, the intrinsic linewidth is large [35].

In order to improve the stability of the laser system and integrate the wavelength selective device into the laser cavity, a distributed Bragg reflector (DBR) was proposed [36]. The DBR-type cavity is designed based on the FP cavity, and a periodic passive Bragg structure is used instead as a mirror to provide wavelength selective optical feedback. The DBR type cavity has certain filtering characteristics due to the periodic

perturbation by the Bragg structure. Combined with the large longitudinal mode spacing brought by the short cavity, it is easy to attain a single longitudinal mode.

By combining the Bragg structure with the gain region and adding a phase shift region to the Bragg structure, a distributed feedback (DFB) structure was formed [37]. The DFB structure combines the feedback and amplification parts together, so the structure is more compact and features tighter integration. The introduction of the phase shift region further limits the light field distribution, so that the DFB structure can overcome the defects of wavelength drift and mode hopping of the DBR structure and works more stably.

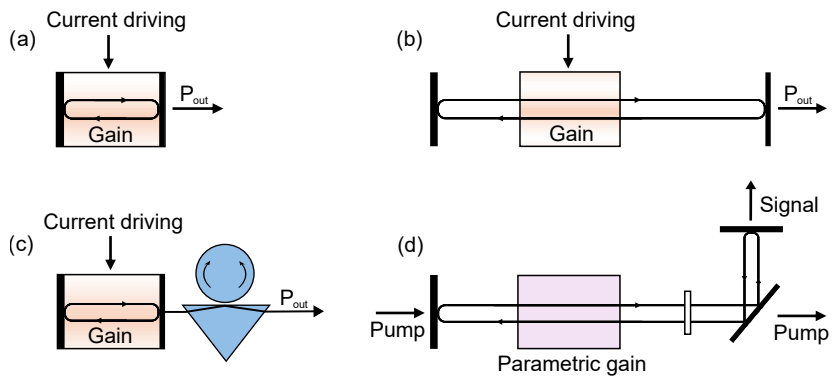

Figure 1.1: (a) Schematic of a conventional semiconductor laser. (b) Schematic of an external cavity semiconductor laser. (c) Schematic of a self-injection locked semiconductor laser. The blue structure represents a microsphere resonator with a coupling element. The microsphere resonator can provide a weak feedback to the semiconductor laser due to backscattering. (d) Schematic of an OPO with an external cavity. The solid black rectangles represent optical mirrors. The smaller hollow rectangle in (d) represents the frequency selective optical component.

Limited by the short cavity length and high absorption loss of active materials, the linewidth of short-cavity semiconductor lasers based on intracavity feedback is still higher than kHz [38, 39]. In order to reduce the laser linewidth, researchers introduced an external passive cavity structure [40, 41]. Based on the semiconductor gain chip, the cavity is extended outside the laser chip by using external mode selection elements or reflectors shown in Fig. 1.1(b). Compared with the intracavity feedback semiconductor laser, an external cavity can obtain narrower linewidth and wider wavelength tuning range by relying on its

longer cavity length and more flexible tuning components in the external cavity. In 1993, researchers achieved a fine adjustment of the laser frequency by fine-tuning the external cavity length [42]. In other work, through special designs of the external cavity, the intrinsic linewidth of semiconductor lasers can be suppressed to kHz or below [43, 44].

In the 1980s, the self-injection locking (SIL) mechanism was also proposed [45, 46]. This method introduces a weak external optical feedback to interfere with the light in the laser cavity. The two signals will be phase coupled and the laser frequency will be locked to the feedback, which can effectively reduce the random drift and noise of the laser frequency and prevent the laser from changing its frequency during the excitation process. With the development of semiconductor laser technology, self-injection locking technology has been increasingly used in semiconductor lasers. Researchers achieved self-injection locking in semiconductor lasers, as shown in Fig. 1.1(c). By introducing an optical feedback from a microresonator into the laser cavity, the output frequency of the laser can be well stabilized and the linewidth can be significantly reduced [47]. With the continuous reduction of optical losses in microresonators, self-injection-locked semiconductor lasers are capable of achieving intrinsic linewidths at the sub-hertz level [32].

Narrow-linewidth optical parametric oscillators

Thanks to the intrinsic broadband tunability and the indirect inheritance of pump coherence, OPOs have become an important alternative for achieving high-performance, narrow-linewidth light sources. Over the past several decades, a variety of techniques for narrowing the linewidth of OPOs have been extensively investigated and developed.

One of the most widely used approaches is injection seeding [48, 49]. In this technique, light from a seed laser, typically a single-frequency continuous-wave source, is injected into a Q-switched slave laser. In the absence of seeding, the slave laser generally oscillates on multiple cavity modes with comparable gain, leading to mode competition. When the seed frequency is sufficiently close to the resonance frequency of a specific cavity mode, that mode experiences preferential amplification and dominates the oscillation, thereby significantly suppressing competing modes. As a result, the emission linewidth is dramatically reduced compared with free-running operation. Consequently, employing a narrow-linewidth pump can effectively suppress the linewidths of the parametric outputs. For example, Ref. [48] reports a 52-fold reduction in the signal

linewidth using this approach.

An alternative method for linewidth narrowing involves incorporating frequency-selective elements into the OPO cavity, such as volume Bragg gratings (VBGs) [50–52] or intracavity etalons [29, 53–59], as illustrated in Fig. 1.1(d). These approaches are similar to external-cavity techniques. VBGs provide narrowband reflection for the signal or idler waves, enabling purely singly resonant OPO operation. Compared with conventional mirror output coupling, linewidth reductions of up to 80-fold have been achieved for the signal wave [51]. Intracavity etalons, which form FP cavities with resonant frequencies controlled by their thickness and incidence angle, can also reduce the output linewidth [57]. Furthermore, by tuning the temperature of the nonlinear gain medium, OPOs can achieve sub-micron wavelength tunability while maintaining narrow linewidth operation [29, 58].

Integrated narrow-linewidth optical sources

With the maturity of micro-nano processing technologies, optical waveguide platforms such as silicon (Si) [60–62], silicon nitride (Si_3N_4) [63–68], silicon oxide (SiO_2) [69, 70], III-V materials [71, 72], lithium niobate [73, 74] and so on, have been greatly developed and provided low-loss propagation. Among them, Si_3N_4 platform has relatively low waveguide loss, low thermo-optical coefficient, compatibility with complementary metal–oxide–semiconductor (CMOS) processes, no influence of two-photon absorption in the telecommunications window, and high Kerr nonlinearity. Despite these advantages of Si_3N_4 in passive photonic components, it has an indirect bandgap and presents many issues when considering active photonic components such as lasers.

So far, the common approach is hybrid integration or heterogeneous integration, combining active photonic components with passive devices in Si_3N_4, Si, etc. Hybrid integration is the process that connects multiple fully processed chips into a single package at the final packaging stage [75–78]. The advantage is that the devices can be tested and characterized before integration. Heterogeneous integration is a process of bonding unpatterned thin films to a Si or Si_3N_4 wafer in a coarse alignment manner and then processing the entire wafer [79–81]. This process technology achieves wafer-level manufacturing, and avoids coupling alignment problems between different structures, thereby improving integration density and cost-effectiveness.

In recent years, researchers have used the above hybrid integration

to make a passive external cavity on Si_3N_4 chips and package them together with active chips, using the ultra-low loss of Si_3N_4 external cavity to help reduce the laser intrinsic linewidth to tens of hertz [75, 76, 82]. The on-chip external cavity still uses the relevant technical principles of the mentioned external cavity, but on-chip integration makes the laser system more compact, stable, and also makes the narrow-linewidth lasers with external cavities more practical.

In addition, by using self-injection locking technology to provide a weak feedback for semiconductor lasers through a low-loss Si_3N_4 microresonator, the intrinsic linewidth of the laser can be suppressed to below 1 Hz [77, 83], which is comparable to low-noise fiber lasers. Moreover, if heterogeneous integration technology and dispersion-engineered Si_3N_4 microresonators are used, narrow-linewidth OPOs can be directly realized on a single chip [84]. In this case, the integration of III-V lasers with Si_3N_4 microresonators can provide higher stability and additional functions, compared with a single III-V laser [31, 85–88].

Beyond III–V materials, doped platforms have also attracted significant attention. A long doped waveguide can function as an amplifier [89], and when incorporated into a cavity, it can operate as a laser [90]. Thanks to their broad gain bandwidth covering the telecom C- and L-bands (1525–1565 nm and 1565–1610 nm, respectively) [91], erbium-doped waveguide devices have been intensively studied over the past two decades [92, 93]. Erbium ions can be incorporated into a variety of low-loss photonic platforms, including Si_3N_4 [94, 95], lithium niobate [96, 97], aluminum oxide (Al_2O_3) [98], and tantalum pentoxide [99], among others. With the continual reduction in device size and energy requirements, it has become feasible to pump on-chip devices using a single diode laser [100]. Leveraging designs inspired by integrated external cavities and hybrid integration techniques, a fully hybrid erbium-doped laser has been demonstrated, achieving a narrow intrinsic linewidth while covering the C- and L-band tuning range [101].

1.2 This thesis

This thesis mainly focuses on the research of integrated narrow-linewidth optical sources. There are two types of optical sources: lasers that exploit stimulated emission from active materials and optical parametric oscillators that exploit nonlinearities.

First, in order to realize a chip-based narrow-linewidth semiconductor

laser, a low-loss passive external cavity can be used to increase photon lifetime, or self-injection locking can be used to provide a weak optical feedback for semiconductor lasers to stabilize the generated frequencies. In either case, an integrated platform with ultra-low propagation loss is required. Therefore, based on the existing ultra-low loss silicon nitride platform, we tried to reduce the roughness of the waveguide sidewall by depositing a thin blanket layer after dry etching, to further decrease the waveguide loss [Paper A].

In addition, to achieve a high performance optical parametric oscillator, the microring resonator is usually put very close to the bus waveguide, the intrinsic loss of the microring will be high due to the extra parasitic loss. Through the bound states in the continuum effect, high intrinsic Q factors or high ratio of intrinsic Q to extrinsic Q can be achieved at some specific wavelengths [102]. By periodically modulating the waveguide loss, mode competition is suppressed, thereby realizing a high-power on-chip optical parametric oscillator [Paper B].

As mentioned above, self-injection locking technology is often used to realize narrow linewidth semiconductor lasers, but whether it can be used for an OPO remains a question. One of the frequencies filtered out from a microcomb-based OPO is fed back to the silicon nitride microring via an optical fiber. By self-injection locking the frequency, its frequency noise is diluted by the low-loss long optical fiber, thereby suppressing the intrinsic linewidth of the frequency [Paper C].

Finally, a chip-scale narrow-linewidth OPO is more promising. Based on [Paper C], integrated components and a meter-level feedback waveguide are designed and manufactured in ultra-low loss silicon nitride. One of the generated frequencies is filtered and routed back into the system through the long feedback waveguide, with its intrinsic linewidth determined by the waveguide length and propagation loss. Both the frequency and feedback strength can be precisely controlled, enabling a fully tunable narrow-linewidth OPO [Paper D].

Thesis outline

In this thesis, Chapter 2 introduces the fundamentals of frequency noise and linewidth, analyzes the noise limits of two types of optical coherent oscillators (semiconductor lasers, soliton microcombs), calculates thermorefractive noise of microresonators and shows the self-heterodyne method for measuring linewidth. Chapter 3 discusses two types of external cavities, with a focus on integrated external cavity designs based

on long waveguides and microring resonators, and provides calculations of their intrinsic linewidths. Chapter 4 demonstrates self-injection locking both theoretically and experimentally. Chapter 5 briefly introduces waveguide loss limitations, ultra-low loss silicon nitride process flow, and considerations for manufacturing long waveguides in silicon nitride. Chapter 6 summarizes the thesis and outlines future research directions.

Chapter 2

Frequency noise in optical coherent oscillators

This thesis focuses on the development of optical coherent oscillators with narrow linewidth. In spite of its intuitive character, the definition of the laser linewidth is an aspect that still today sparks significant interest in the community and does not have a single unique metric for its characterization. In this chapter, we will discuss the main concepts that permit analyzing the frequency noise of optical coherent oscillators, and the self-heterodyne technique used to measure quantitatively the linewidth of our lasers. Therefore, this chapter provides the theoretical foundation for establishing a comparative and quantitative assessment of laser linewidth among different optical coherent oscillators.

2.1 Frequency noise

In practice, the amplitude, phase, and frequency of an oscillator are never perfectly constant; instead, they exhibit irregular fluctuations over time that are typically too complex to be described by a simple analytical function. These unwanted variations are commonly referred to as noise or jitter. To quantitatively characterize such fluctuations, statistical methods are required, providing the foundation for analyzing oscillator stability and frequency noise.

2.1.1 Basics of frequency noise

In the optical oscillator model, the instantaneous output electric field and instantaneous frequency of the optical oscillator are written as [103]

$$E(t) = (|E_0(t)| + |\Delta E_0(t)|) \cdot \exp[j2\pi\nu_0 t + j\Delta\phi(t)], \tag{2.1}$$

$$\nu(t) = \nu_0(t) + \Delta\nu(t) = \nu_0(t) + \frac{\mathrm{d}\Delta\phi(t)}{2\pi \mathrm{d}t}. \tag{2.2}$$

$|E_0(t)|$ represents the amplitude of the electric field. $|\Delta E_0(t)|$ represents the random amplitude fluctuation around $|E_0(t)|$. Similarly, $\Delta\phi(t)$ and $\Delta\nu(t)$ are the random phase and frequency fluctuation, respectively. ν_0 is the center optical frequency of the oscillator.

The power spectral density (PSD) is a time-domain statistical representation of a random process - the Fourier transform of the autocorrelation function which reveals the similarity of the noise state at adjacent moments. So the stability of physical quantities such as intensity, frequency, and phase is usually expressed in the frequency domain by their PSD $S(f)$. The PSD represents the distribution of the average power of a physical quantity over a certain period of time as the Fourier frequency changes. It represents the power carried per unit frequency, in units of power per hertz [104].

$$R_\nu(\tau) = \lim_{T\to\infty} \int_{-T}^{T} \Delta\nu(t+\tau)\Delta\nu(t)dt. \tag{2.3}$$

$$\begin{aligned} S_\nu(f) &= \int_0^\infty R_\nu(\tau)\exp(-j2\pi f\tau)d\tau \\ &= 2\int_{-\infty}^{\infty} R_\nu(\tau)\exp(-j2\pi f\tau)d\tau. \end{aligned} \tag{2.4}$$

$$S_\nu(f) = f^2 S_\phi(f). \tag{2.5}$$

$R_\nu(\tau)$ is the autocorrelation function of the frequency fluctuation $\nu(\tau)$. In practice, we are only interested in the positive Fourier frequencies f, so here, $S_\nu(f)$ is the single-sided PSD of the frequency fluctuation. The PSD of the phase fluctuation $S_\phi(f)$ has a similar definition [104].

If the PSD is integrated over the entire frequency range, the total average power can be obtained. In essence, it reflects that the energy of different frequency components that constitute the signal is generally different, that is, the contribution of signal components of different frequencies to the total energy of the signal is generally unequal. This is why in the frequency domain the concept of spectral density is used to describe stability rather than spectrum. The former has direct physical meaning within a finite measurement time and can be directly measured, while the latter only exists in theoretical analysis of infinite time samples and will not converge once the samples are truncated within a finite time, making it difficult to obtain directly in actual measurements [103].

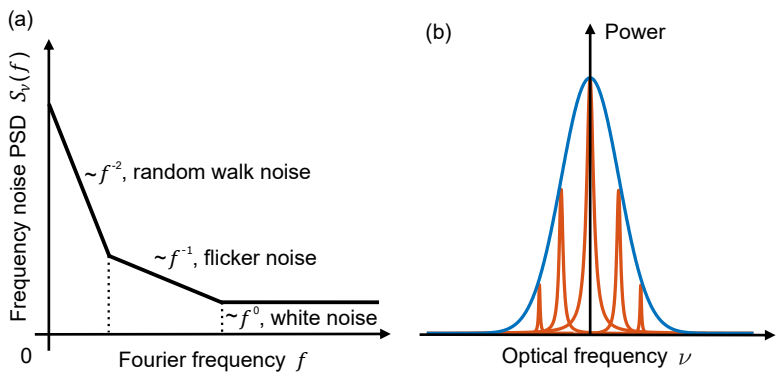

Figure 2.1: (a) Schematic of the frequency noise PSD of a single-frequency laser. Random walk noise and flicker noise dominate in the low frequency range (long-term stability), while white noise dominates in the high frequency range (short-term stability). Both axes are plotted on a logarithmic scale. (b) Schematic of the laser spectrum. At short time scales, the frequency spectrum is mostly a Lorentzian and very narrow (orange curves), while at longer time scales, when flicker noise kicks in, the centroid of the Lorentzian changes over time and the frequency spectrum looks broader, with a profile that resembles more a Voigt function (blue curve).

Typically, the frequency noise PSD $S_\nu(f)$ can be reasonably modeled by the superposition of three independent frequency noise processes that follow a power law with integer exponent $0 \leq \alpha \leq 2$ [103],

$$S_\nu(f) = \sum_{\alpha=0}^{2} h_\alpha f^{-\alpha}. \tag{2.6}$$

In the Fig. 2.1(a), the frequency noise PSD is divided into different regimes [105]. The contribution of low Fourier frequencies decreases

with increasing frequency and includes random walk noise and flicker noise (also called 1/f noise). In the high frequency regime, PSD of the frequency fluctuations is usually independent of frequency and called white noise. For lasers, the random walk noise is caused by the influences of environment like temperature, vibrations. The flicker noise can be introduced by thermal noise within the laser cavity. The white noise is caused by the random processes of spontaneous emission and carrier fluctuations [103].

2.1.2 Spectral line shape

Due to the frequency noise, the optical frequency spectrum distribution of a laser is no longer an ideal single line, but extends to both sides of the optical carrier frequency in the form of modulated sidebands, as shown in Fig. 2.1(b). Knowing the frequency noise PSD allows us to recover the laser line shape and thus the linewidth. Therefore, the relationship between the frequency noise PSD and the laser linewidth is discussed below.

By integrating over the full Fourier frequency range, the laser light field PSD or the laser line shape can be calculated directly from the laser frequency noise as follows [105–107]

$$S_E(\nu) = E_0^2 \int_0^\infty \cos[2\pi(\nu - \nu_0)\tau] \times \exp[-2 \int_0^\infty S_\nu(f) \frac{\sin^2(\pi f \tau)}{f^2} df] d\tau, \tag{2.7}$$

where $S_E(\nu)$, $S_\nu(f)$ are the single-sided PSD of electric field and frequency noise, respectively.

In the absence of low frequency noise, $S_\nu(f) = h_0$ Hz^2/Hz and

$$S_E(\nu) = E_0^2 \frac{h_0}{(\nu - \nu_0)^2 + (\pi h_0/2)^2}. \tag{2.8}$$

It leads to the Lorentzian line shape with a full width at half-maximum (FWHM) of πh_0 Hz. The Lorentzian linewidth is also referred in the literature as fundamental linewidth or intrinsic linewidth [105].

If there is high frequency noise, in the low frequency region,

$$S_E(\nu) = E_0^2 (\frac{2}{\pi h_0 f_c})^{1/2} \exp[-\frac{(\nu - \nu_0)^2}{2 h_0 f_c}], \tag{2.9}$$

where f_c is cutoff frequency. The line shape is Gaussian with a FWHM of $[8\ln(2) h_0 f_c]^{1/2}$ Hz, which depends on the cutoff frequency [106].

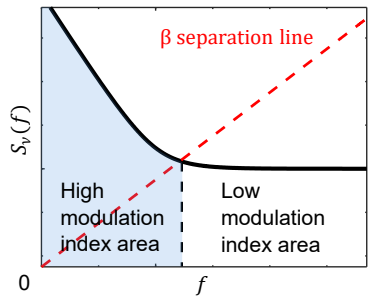

Figure 2.2: Frequency noise PSD of a single-frequency laser. Both axes are plotted on a logarithmic scale.

Combining the influence of the above frequency noises, the overall line shape has a Voigt-like profile [108]. The FWHM of the Voigt profile is called integrated linewidth [106]. The actual noise spectrum of a laser is much more complex and produces line shapes that cannot be resolved and can only be determined by numerical methods. According to [106], the frequency noise PSD can also be divided into two regions using an approximate line (β separation line). As shown in Fig. 2.2, in the first region, $f < 8\ln(2) \cdot S_\nu(f)/\pi^2$ and the noise level is high compared to the Fourier frequency f. It contributes more to the integrated linewidth, this is to say, it provides a high modulation index. While $f > 8\ln(2) \cdot S_\nu(f)/\pi^2$, the noise contributes to the wings of the Lorentzian line shape or the intrinsic linewidth. The modulation speed of the frequency noise is too fast to have a significant effect on the integrated linewidth. The approximate value of the integrated linewidth follows the formula:

$$\mathrm{FWHM} = [8\ln(2)A_s]^{1/2}, \tag{2.10}$$

where A_s is the surface area of the high modulation index area (shaded area in Fig. 2.2).

Fig. 2.3 shows the frequency noise PSD of an external cavity semiconductor laser (CTL 1550) from TOPTICA measured using self-heterodyne method. It can be seen from the figure that the PSD value tends to be flat after 50 kHz. By calculating the average value of PSD from 50 kHz to 10 MHz as h_0, the intrinsic linewidth of this laser is around 190 Hz. Then calculate the shaded area and use Eq. 2.10 to get the integrated linewidth of 179 kHz. It can be said that the frequency noise PSD is convenient to assess the linewidth dynamics at different time scales.

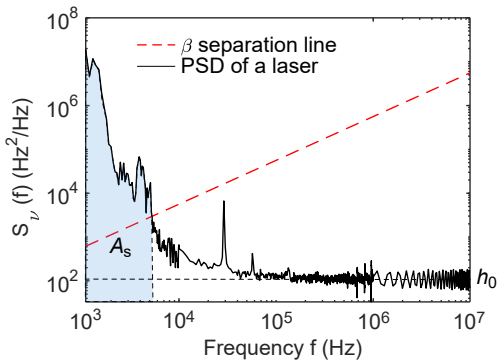

Figure 2.3: Measured single-sided frequency noise PSD of a semiconductor laser.

2.2 Frequency noises of optical coherent oscillators

For high-speed applications such as data communications, the laser noise characteristics at high frequencies are more important because this noise regime mainly affects the phase error variance of the coherent communication link [109]. In this case, the intrinsic linewidth is more applicable. The target topic discussed in this thesis is the intrinsic linewidth. Therefore, the influencing factors and calculation of the intrinsic linewidth of semiconductor lasers and optical parametric oscillators will be introduced below.

2.2.1 Frequency noise of semiconductor lasers

The linewidth of a single-frequency laser is determined by the quantum process of spontaneous emission. Each photon emitted spontaneously into the laser mode can induce stimulated emission and the resulting field amplitude is added to the field in the laser. Due to the statistical fluctuation contribution of the spontaneously emitted photons, the phase of the optical field in the laser cavity will fluctuate greatly, resulting in a large intrinsic linewidth [3].

Firstly, assuming that the laser is based on a FP cavity, the steady-state condition for the laser cavity is given by [110, 111]

$$r_1 r_2 \exp[2jkL + (g - \alpha_c)L] = 1, \tag{2.11}$$

where r_1, r_2 are the electric field reflectivities of the front and back facet,

k is the propagation constant, L is the physical length of the cavity, g is the modal gain and α_c is the loss due to absorption and scattering in the laser medium. From the real part of the above formula, the threshold modal gain g_{th} can be written by

$$\begin{aligned} g_{\text{th}} &= \alpha_c + \frac{1}{L}\ln(\frac{1}{r_1 r_2}) \\ &= \alpha_c + \alpha_m = \alpha_{\text{tot}}, \end{aligned} \tag{2.12}$$

where α_m is the facet loss of the two mirrors.

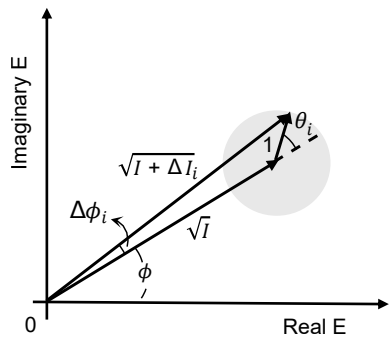

Figure 2.4: Vector-based description of the electric field under noise perturbation. I and ϕ represent the intensity and phase of the electric field, respectively. The initial electric field $E = \sqrt{I} \cdot \exp(j\phi)$, the random change $\Delta E = \exp(j\theta_i)$ caused by the i-th spontaneous radiation, and unit amplitude fluctuation is assumed. The instantaneous electric field $E = \sqrt{I + \Delta I_i} \cdot \exp(j\phi + j\Delta\phi_i)$.

Fig. 2.4 shows the electric field vector of each photon. The shaded area represents the random electric field fluctuation of the photon, including amplitude and phase fluctuations. The phase change $\Delta\phi_i$ of the photon is the result of the combined effect of the random phase change θ_i and the delayed phase change caused by the instantaneous change of the field intensity.

From a physical standpoint, the phase of the photon electric field is related to the real part of the medium's refractive index, while the imaginary part of the medium's refractive index affects the intensity of the photon electric field by affecting the net gain. Therefore, the phase change of the photon electric field in a laser is related to the changes in both the real and imaginary parts of the medium's refractive index, and the phase change caused by the change in light intensity or the imaginary part of the refractive index is additional.

In semiconductor lasers, the intensity change or the photon number change caused by spontaneous emission will cause a change in the carrier density of the semiconductor active medium, and the carrier density change modifies the refractive index of the medium, thereby introducing the additional phase change. Compared with other types of lasers whose intensity fluctuation has little effect on the refractive index, the coupling between the amplitude and phase of the electric field is more pronounced in semiconductor lasers [110]. In this sense, this is the reason why the intrinsic noise or linewidth of semiconductor lasers is enhanced.

Here, a linewidth enhancement factor α is introduced as [35, 112]

$$\alpha = \frac{\Delta n_{\text{real}}}{\Delta n_{\text{imag}}}. \tag{2.13}$$

Δn_{real}, Δn_{imag} are the fluctuations of the real and imaginary part of the refractive index $n = n_{\text{real}}$ - jn_{imag}. α is related to the active medium.

After a series of deductions, the intrinsic linewidth of semiconductor laser becomes [35, 113, 114]

$$\Delta\nu = \frac{v_{\text{g}}^2 h\nu_0 n_{\text{sp}} \alpha_m \alpha_{\text{tot}} (1+\alpha^2)}{4\pi P_{\text{tot}}}, \tag{2.14}$$

where v_{g} is the group velocity of the laser, and h is the Planck constant ($6.62607015 \times 10^{-34}\text{J} \cdot \text{s}$). n_{sp} is the spontaneous emission factor, whose physical meaning is the proportion of spontaneous emission entering the laser modes [104]. α_c and α_{tot} are the propagation loss and total loss of the laser cavity, respectively, as shown in Eq. 2.12. P_0 is the output power per facet, and the total output power $P_{\text{tot}} = 2P_0$, if $r_1 = r_2$.

In order to obtain a narrow linewidth for a given output power, α_m and α_c should be as low as possible [115]. According to Eq. 2.12, if the reflectivities of two facets r_1, r_2 are unchanged, extending the cavity length L can effectively reduce α_m. Additionally, α_c is the propagation loss of the cavity, which depends strongly on the material, design and manufacturing method. Decreasing the propagation loss can also reduce the laser intrinsic linewidth. Chapter 3 analyzes the case where a low-loss dielectric external cavity is used to decrease the linewidth of semiconductor lasers.

2.2.2 Frequency noise of optical parametric oscillators

Since the lasing wavelength of a laser depends on the bandgap of the active material, currently relying solely on lasers as light sources may

not be able to cover the entire optical band, which limits optical applications and researches. An OPO is based on optical parametric amplification, and its gain wavelength is no longer limited by the material bandgap, so the optical bands that cannot be covered by lasers can be achieved by OPOs. As a special and practical OPO, a microcomb has been increasingly studied. Microcombs are optical frequency combs generated in a nonlinear high-Q microcavity, which is widely used in high-precision time and frequency measurement, optical communication and other fields [116–118]. It uses four-wave mixing (FWM) to generate multiple equally spaced frequencies [119].

Conventional frequency combs are based on mode-locked lasers [120], where the gain of a conventional frequency comb comes from stimulated emission in the active gain medium, so its intrinsic linewidth is partially determined by spontaneous emission. In contrast, the gain of soliton microcombs is based on optical parametric amplification, and the noise caused by spontaneous scattering is very weak. The pump laser is added to the microcombs in a coherent manner, so its noise is uniformly transmitted to all comb lines [121].

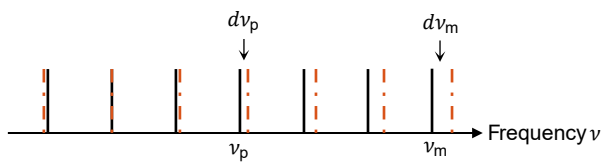

Figure 2.5: Schematic of the comb line distribution and the repetition rate change caused by the change of pump frequency. ν_p, ν_m are the frequencies of pump and m-th comb line. The black line segments represent the initial comb lines, and the red dashed line segments represent the comb lines after the pump frequency is shifted.

Fig. 2.5 shows the distribution of the comb lines. The frequency of the m-th comb line can be expressed as

$$\nu_m = \nu_p + m\nu_{\text{rep}}, \tag{2.15}$$

where m is counted from the pump, and ν_p, ν_{rep} are the pump frequency and the repetition rate of the frequency comb. If the repetition rate remains exactly the same, the pump frequency noise will be transferred to each comb line. However, the pump frequency noise can also affect the repetition rate due to intrinsic intra-pulse Raman scattering [122] and dispersive wave recoil [123]. Therefore, a linear perturbation on Eq.

2.15 results into

$$d\nu_m = d\nu_p(1 + m\frac{d\nu_{\text{rep}}}{d\nu_p}), \tag{2.16}$$

where $d\nu_p$ is the pump frequency fluctuation, $d\nu_m$ and $d\nu_{\text{rep}}$ are the changes in m-th comb line frequency and repetition rate caused by pump frequency fluctuation. As shown in Fig. 2.5, for comb lines with higher frequencies than the pump, the frequency offset increases with increasing frequency. On the other side of the pump, there may be some comb lines with a smaller frequency offset than the pump.

Because the PSD (calculated by Eq. 2.4) can be used to calculate the linewidth of an optical source, the frequency noise PSD of the m-th comb line $S_{\nu,m(f)}$ is calculated as [124]

$$S_{\nu,m}(f) = S_{\nu,p}(f)(1 + m\frac{d\nu_{\text{rep}}}{d\nu_p})^2. \tag{2.17}$$

$S_{\nu,p}(f)$ is the PSD of the pump frequency noise. It can be seen that the intrinsic linewidth of the microcomb due to pump frequency noise has a parabolic relation with the comb line number.

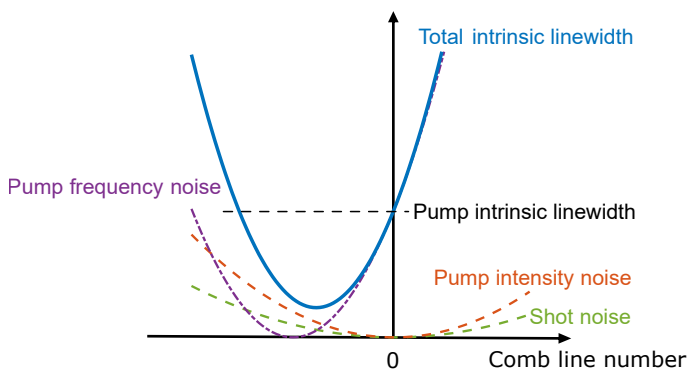

Figure 2.6: Schematic of intrinsic linewidth contribution of a soliton microcomb. Comb line 0 represents the pump frequency.

In addition to the pump frequency noise, the pump intensity noise and shot noise also affect the intrinsic linewidth of the comb lines. As shown in Fig. 2.6, the three noise sources are independent of each other and all introduce a parabolic distribution to the intrinsic linewidth [124–126]. The difference is that the linewidth distribution caused by the pump intensity noise and the shot noise is symmetric about the pump frequency, and the two contributions are usually weaker than the pump

frequency noise. After adding them together to get the total intrinsic linewidth, there will still be some comb lines with an intrinsic linewidth narrower than the intrinsic linewidth of the pump frequency.

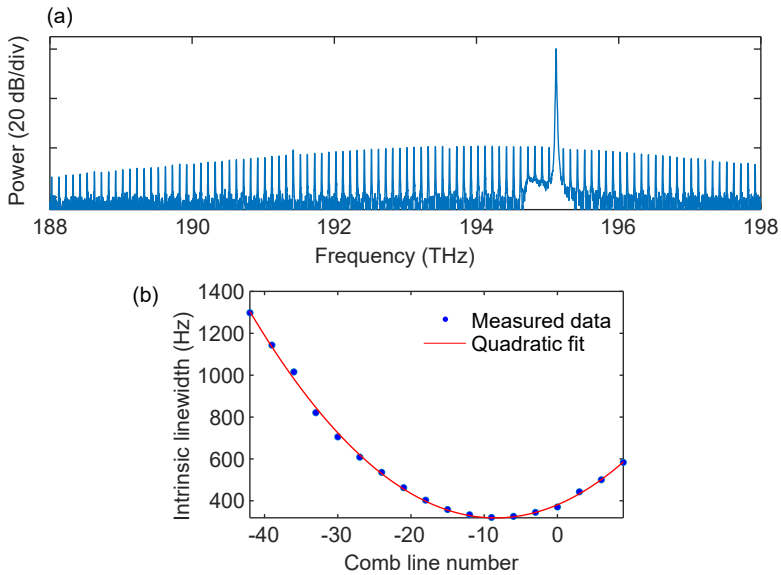

Figure 2.7: (a) Frequency spectrum of a soliton microcomb. (b) Measured and fitted intrinsic linewidth distribution.

Fig. 2.7 shows the optical spectrum and corresponding intrinsic linewidth distribution of a soliton microcomb generated on a Si_3N_4 microring resonator with a free spectral range (FSR) of 100 GHz. Since a sufficient power is required for linewidth measurement, an erbium-doped fiber amplifier (EDFA) is used to amplify the power of the comb lines. The total number of comb lines which can be measured is limited by the bandwidth of the EDFA. Nevertheless, comb lines from -42 to 9 can be measured. One can see that the intrinsic linewidth has an almost perfect parabolic profile, and the intrinsic linewidths of comb lines -16 to -1 are below that of the pump frequency.

In [Paper C], a soliton frequency comb generated by pumping a silicon nitride micro-ring resonator exhibits an intrinsic linewidth that follows a parabolic distribution. Since the pump linewidth is determined by the pump laser itself, modifying the linewidth of any individual comb line, while the overall distribution obeys the parabolic profile, will lead to a redistribution of the linewidths of the other comb lines. By filtering out a comb line and reinjecting it into the comb after propagation through

a low-loss external cavity, the frequency noise of that comb line can be diluted by the external cavity, thereby reducing its linewidth to the sub-hertz level. The linewidth of this selected comb line can thus become significantly narrower than that of the pump and represents the narrowest linewidth across the entire comb. If the selected frequency is far from the pump frequency, a broad spectral region around this frequency can achieve linewidths narrower than that of the pump. In this way, a multi-wavelength optical source featuring both ultralow linewidth and broad bandwidth can be realized.

2.2.3 Thermorefractive noise of microresonators

Optical microresonators, owing to their small mode volume and high quality factor, have found wide applications in lasers and OPOs [127]. However, their frequency stability is severely limited by thermal noise, particularly thermorefractive noise (TRN), which originates from fluctuations of the refractive index caused by temperature fluctuations in the material. In the following, focusing on Si_3N_4 microring resonators, the theoretical modeling of TRN is analyzed based on a thermal noise model under the assumption of an infinite heat bath [128, 129].

The model assumes that the microresonator material is homogeneous and that the optical mode field distribution is known; the resonator is embedded in an infinite thermal bath with a constant ambient temperature; temperature fluctuations arise solely from the intrinsic thermodynamic fluctuations of the material [130]. Under these assumptions, the single-sided PSD of the effective temperature fluctuations can be approximately expressed as

$$S_T(\omega) = \frac{k_B T^2}{\sqrt{\pi^3 \kappa \rho C \omega}} \sqrt{\frac{1}{2p+1}} \frac{1}{R\sqrt{d_z^2 - d_r^2}} \frac{1}{[1 + (\omega \tau_d)^{3/4}]^2}, \tag{2.18}$$

where T is the temperature, ω is angular frequency, κ_B is Boltsman's constant (1.380649×10^{-23} J/K), κ is the thermal conductivity, ρ is the material density, C is specific heat capacity, R is the radius of the microcavity. In spherical whispering-gallery-mode (WGM) microresonators, orbital number l, azimuthal mode number m and meridional mode number p satisfy $p = l - m$. d_r and d_z are halfwidths of the fundamental mode in the radial and azimuthal directions.

In microring resonators, $l = m = 2\pi n_{\text{eff}} R/\lambda_0$, where λ_0 is the resonant wavelength, n_{eff} is effective index of the waveguide, and $p = 0$. d_r

and d_z can be estimated from the following expression:

$$d_r \approx \frac{\lambda_0}{2\pi n_{\text{eff}}}\sqrt{\frac{R}{W}}, \tag{2.19}$$

$$d_z \approx \frac{\lambda_0}{2\pi n_{\text{eff}}}\sqrt{\frac{H}{W}}, \tag{2.20}$$

where W, H are the width and height of the waveguide, respectively. And the thermal diffusion time scale τ_d is expressed as

$$\tau_d = \frac{\pi^{1/3}}{4^{1/3}}\frac{\rho C}{\kappa}d_r^2. \tag{2.21}$$

The PSD of the resonance frequency fluctuations induced by temperature fluctuations can be obtained through the following relation:

$$S_\nu(\omega) = (\nu_0\frac{1}{n_{\text{eff}}}\frac{dn}{dT})^2 S_T(\omega), \tag{2.22}$$

where $\nu_0 = c_0/\lambda_0$ is resonant frequency of the microresonator, dn/dT is thermo-optic coefficient.

This model performs well in the systems with homogeneous materials. For Si_3N_4 microresonators on integrated photonic chips, the actual structure involves multiple material regions such as the substrate and cladding and has finite dimensions. Nevertheless, the model remains applicable in the high-frequency regime. Experimental validation in microring resonators has confirmed the effectiveness of its predictions [131].

As shown in Fig. 2.8, the PSDs of TRN of microrings with different FSRs are calculated. A smaller FSR corresponds to a longer waveguide, a larger mode volume, and thus a lower level of TRN. This behavior arises from the fundamental of thermorefractive noise. A larger mode volume means that thermodynamic temperature fluctuations are averaged over a greater number of molecules, reducing their root-mean-square amplitude. Therefore, the frequency noise induced by refractive index fluctuations is overall reduced. In [Paper C], the feedback loop formed by the optical fiber has a much larger mode volume compared to the integrated waveguide loop in [Paper D], resulting in significantly lower TRN in the former.

Besides the radius of microring resonators, the optical confinement of waveguides also determines the effective mode volume. Stronger confinement leads to a smaller mode volume, stronger locality of temperature fluctuations, and therefore larger TRN. The confinement of a waveguide

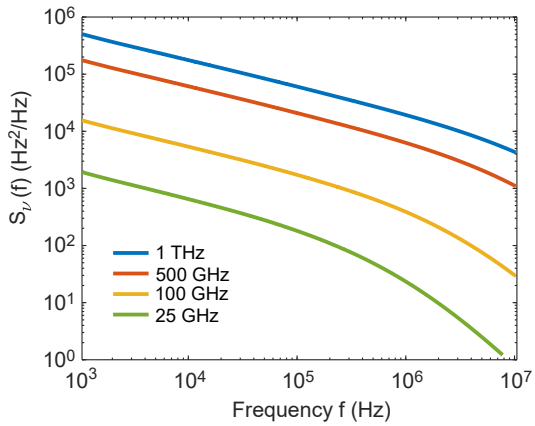

Figure 2.8: Simulation results of thermorefractive noise with the theoretical predictions. Parameters used in the simulation: $\kappa = 30$ W/m/K, $\rho = 3.29 \times 10^3$ kg/m^3, $dn/dT = 2.45 \times 10^{-5}$ K^{-1}, $C = 800$ J/kg/K, $n_{\text{eff}} = 1.84$, $n_{\text{g}} = 2.12$, $T = 296$ K, $\lambda_0 = 1550$ nm, $l = m = 2\pi n_{\text{eff}} R/\lambda_0$. The waveguides have a thickness of 740 nm, and a width of 2.4 μm. The radius $R = c_0/(2\pi n_{\text{g}}\text{FSR})$.

is mainly determined by two key parameters: the geometry and dimensions of the waveguide core, and the refractive index contrast between the core and the cladding. In general, a smaller core size and a larger index contrast lead to stronger confinement, resulting in a reduced mode volume. However, such strong confinement is beneficial for enhancing nonlinear effects and increasing device integration density. As a result, the waveguide design must strike a balance between the two considerations.

Additionally, the thermo-optic coefficient of the material can convert temperature fluctuations into frequency fluctuations. A larger thermo-optic coefficient means that the same temperature variation produces a larger refractive index change, thereby linearly amplifying the frequency noise. The thermo-optic coefficient of Si_3N_4 is relatively small compared to other materials such as silicon [132], which is one of the key reasons why Si_3N_4 is an attractive low-noise photonic platform.

In summary, the design of microresonators must balance geometric parameters and material properties to optimize performance. We need to adjust the radius and waveguide confinement to control the mode volume while selecting materials with low thermo-optic coefficients and low optical loss, in order to minimize thermorefractive noise and other frequency noises.

2.3 Self-heterodyne method

The self-heterodyne method is among the most widely employed techniques for measuring linewidth, particularly for assessing the coherence of optical oscillators [133]. This method is based on the principle of interference, in which the laser signal is compared with a delayed version of itself to extract frequency information. The following section provides an overview of the underlying principle and limitations of this technique.

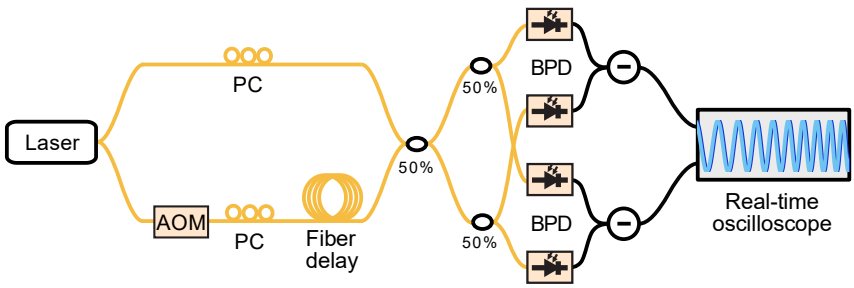

Figure 2.9: Schematic of the self-heterodyne measurement setup. PC: polarization controller, AOM: acousto-optic modulator, BPD: balanced photodetector.

As shown in Fig. 2.9, the laser signal is first split using a beam splitter. One of the split signals is sent directly to the measurement system as a reference. The other path is delayed in time and optionally shifted in frequency by an acousto-optic modulator (AOM). In our experiments, we use the delayed fiber with the length of 1.5 km. The AOM is driven with an 80 MHz radio-frequency carrier, and the sampling rate of the oscilloscope is set to 625 MHz to prevent aliasing. A time delay is introduced in the delayed path, which can be controlled by changing the optical fiber length. The two outputs are split and received by two identical balanced photodetectors (BPDs). Using BPDs helps suppress relative intensity noise and allows for cross-correlation between the electrical outputs, thereby suppressing the independent BPD noise [134]. The two signals interfere with each other and generate a beat signal whose spectral properties depend on the laser linewidth. A wider laser linewidth corresponds to a more significant frequency fluctuation between the two signals. By extracting the phase noise, the frequency noise PSD and the linewidth can be derived [134–136].

According to Eq. 2.3 and Eq. 2.4, in order to obtain frequency noise PSD $S_\nu(f)$, the frequency fluctuation $\Delta\nu(t)$ must be known. The

interference of two signals produces a beat note, from which the phase fluctuation over the time delay can be extracted by Hilbert transform, allowing the frequency noise to be obtained as well. The relationship is given by the following equation:

$$\Delta\nu_\tau(t) = \frac{1}{2\pi}\frac{d\Delta\phi_\tau(t)}{dt}, \tag{2.23}$$

where $\Delta\phi_\tau(t) = \phi(t) - \phi(t-\tau)$, τ is the time delay.

From this, the frequency noise PSD $S_{\nu(\tau)}(f)$ at the given time delay can be calculated. The original frequency noise is then recovered using the processing gain $G(f)$ [134]:

$$S_\nu(f) = G(f)S_{\nu(\tau)}(f), \tag{2.24}$$

$$G(f) = \frac{1}{4\sin^2(\pi f\tau)}. \tag{2.25}$$

$4\sin^2(\pi f\tau)$ is also referred to as the transfer function of the system. This transfer function has zeros at frequencies $f = m/\tau$ (where m is an integer). When a long delay line (large τ) is used, the zeros are densely distributed in the frequency domain, which may result in multiple zeros within the frequency range of interest. In contrast, with a short delay line (small τ), the first zero occurs at a higher frequency (e.g., tens of MHz or above), allowing direct measurement over a wide frequency range (0–10 MHz), which is suitable for broadband noise analysis.

Secondly, the length of the delay line has a significant impact on the sensitivity of low-frequency measurements. In the low-frequency region ($f \ll 1/\tau$), the transfer function can be approximated as $4\pi^2 f^2\tau^2$, which means that its magnitude is proportional to τ^2. This implies that a long delay line provides higher sensitivity to low-frequency noise, allowing more accurate extraction of laser frequency fluctuations in the kHz and sub-kHz range. Conversely, a short delay line has a very small transfer function at low frequencies, requiring extremely high compensation gain to recover the signal. This not only amplifies noise but may also make the measurement sensitive to the resolution bandwidth, potentially causing distortion.

Finally, the length of the delay line also directly affects the sensitivity to environmental disturbances. A long delay line with several kilometers length is highly susceptible to temperature fluctuations, mechanical vibrations, and acoustic noise, which can couple into additional

low-frequency phase noise. To mitigate these effects, acoustic and thermal isolation of the fiber is required, increasing the complexity and cost of the system. In contrast, a short delay line, due to its shorter physical length, is much less sensitive to environmental perturbations and more easily achieves a low-noise baseline.

Overall, the optimal delay line length depends on the specific measurement goals. Employing multiple delay lines can sometimes balance different needs, allowing for a more complete characterization of the frequency noise properties.

Chapter 3

Optical coherent oscillators with external cavities

The intrinsic linewidth represents the fundamental lower limit of a laser's linewidth determined by quantum noise (spontaneous emission). Investigating it helps to elucidate the ultimate coherence limit of lasers, thereby providing guidance for the design of ultra-narrow-linewidth lasers approaching the theoretical limit. In practical experiments, electrical feedback and locking techniques are often used to reduce the linewidth of light sources. They are very effective for reducing low-frequency linewidth, but due to the bandwidth limitations, these techniques are less effective for high frequency noise [105]. Therefore, it is necessary to use optical strategies to suppress the intrinsic noise of light sources. This chapter introduces how external cavities reduce the intrinsic linewidth of optical coherent oscillators.

3.1 External-cavity-induced linewidth reduction

According to the description in Section 2.2.1, the intrinsic linewidth of a semiconductor laser is related to the intracavity propagation loss and cavity length. A longer cavity length has a suppressive effect on the intrinsic noise of a semiconductor laser. However, simply increasing the length of the active media cannot significantly reduce the intrinsic linewidth because the linewidth is still limited by the high propagation loss of active media. Therefore, semiconductor lasers are often combined with low-loss passive external cavities to achieve narrow linewidth.

The configuration of a semiconductor laser with an external cavity is

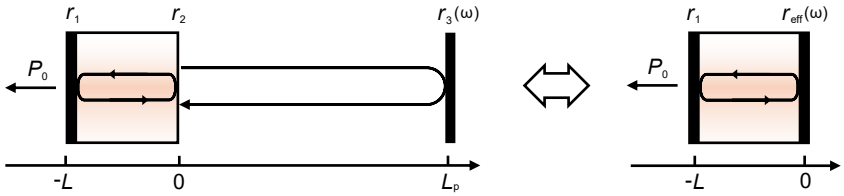

Figure 3.1: Schematic of a semiconductor laser with an external cavity and its equivalent structure. The output power P_0 is emitted from the front mirror. The electric field reflectivities of the laser mirrors and external mirror are r_1, r_2, $r_3(\omega)$. r_1, r_2 may have weaker wavelength dependence, but we ignore it here. The physical length of the laser cavity is L and the passive external cavity is L_p.

shown in Fig. 3.1. The external mirror can be expressed by $r_3(\omega)$ which could be a frequency-dependent electric field reflectivity [137], such as Bragg grating [81], multiple microrings [79], and so on. Generally, the propagation loss of the external cavity is much lower than that of the laser waveguide. Compared to simple FP lasers, the complexity of the external cavity is relatively high. In order to use the theoretical predictions in Section 2.2.1, the passive external cavity can be replaced by an effective mirror with a complex wavelength dependence, denoted as [105]

$$\begin{aligned} r_{\text{eff}}(\omega) &= t_2^2 \cdot t_{\text{passive}}(\omega)^2 \cdot r_3(\omega) \\ &= (1 - r_2^2) \cdot \exp(-j\omega\tau_p - \alpha_p L_p) \cdot r_3(\omega), \end{aligned} \tag{3.1}$$

where τ_p is the round-trip time of the external cavity. The propagation loss of the passive external cavity is α_p. The effective reflectivity r_{eff} is the transfer function of the round-trip transmission of the entire passive cavity. This term can be separated into amplitude and phase as

$$r_{\text{eff}}(\omega) = |r_{\text{eff}}(\omega)| \exp[j\varphi_{\text{eff}}(\omega)]. \tag{3.2}$$

And the total losses of the semiconductor laser is

$$\begin{aligned} \alpha_{\text{tot}} &= \alpha_c + \alpha_m \\ &= \alpha_c + \frac{1}{L}\ln(\frac{1}{r_1\,|r_{\text{eff}}(\omega)|}). \end{aligned} \tag{3.3}$$

According to Eq. 2.14 in Chapter 2, combined with the above effective reflectivity, the intrinsic linewidth becomes [33, 105, 137]

$$\Delta\nu = \frac{v_g^2 h\nu_0 n_{\text{sp}} \alpha_m \alpha_{\text{tot}}(1+\alpha^2)}{4\pi P_0 \left[1 + \frac{r_1}{|r_{\text{eff}}(\omega)|}\frac{1-|r_{\text{eff}}(\omega)|^2}{1-r_1^2}\right]} \cdot \frac{1}{F^2}, \tag{3.4}$$

where P_0 is the output power emitted by the front mirror with reflectivity r_1. Due to the frequency dependence of the phase and reflectivity of the external cavity, the intrinsic linewidth is reduced by F^2 [82, 138].

$$F = 1 + A + B, \tag{3.5}$$

where

$$A = \frac{1}{\tau_0} \frac{d\varphi_{\text{eff}}(\omega)}{d\omega}, \tag{3.6}$$

$$B = \frac{\alpha}{\tau_0} \frac{d(\ln |r_{\text{eff}}(\omega)|)}{d\omega}. \tag{3.7}$$

$\tau_0 = 2L/v_{\text{g}}$ is the round-trip time in the semiconductor laser cavity. A can be thought of as the ratio of the round-trip times between the passive external cavity and the laser cavity. From this perspective, the longer the passive cavity, the stronger the linewidth suppression. Due to the existence of the factor α, B will only appear when α is non-zero. B represents the additional linewidth suppression mechanism based on the coupling of light field intensity and phase in semiconductor lasers [82].

3.2 Long-waveguide-based external cavity

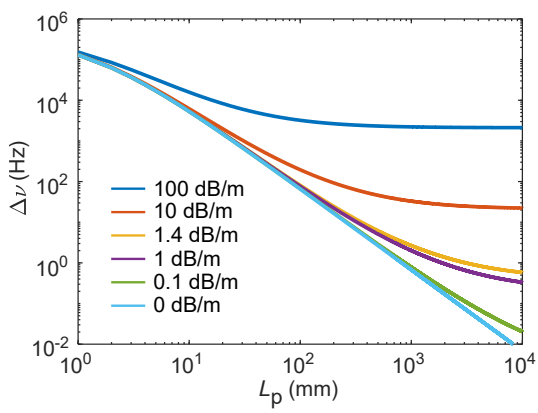

Figure 3.2: Intrinsic linewidth calculation based on different external cavity losses α_p and lengths L_p. Parameters used in the simulation: $\alpha = 5$, $n_{\text{sp}} = 2$, laser wavelength $\lambda = 1550$ nm, output power $P_0 = 1$ mW, length of active part $L = 0.7$ mm, group index $n_{\text{g,active}} = 3.6$, $n_{\text{g,passive}} = 2$, reflection coefficients $r_1 = 0.9$, $r_2 = 0.9$, $r_3 = 1$, propagation loss of active part $\alpha_c = 13$ cm^{-1}.

Consider a semiconductor laser with a long external waveguide and a frequency-independent external mirror ($dr_3(\omega)/d\omega = 0$, $d|r_{\text{eff}}(\omega)|/d\omega = 0$, $B = 0$). Based on Eq. 3.4, the intrinsic linewidth of that laser can be calculated. As shown in Fig. 3.2, for the same waveguide loss, the intrinsic linewidth decreases as the external cavity becomes longer, which is consistent with the above discussion.

However, the suppression is finally limited by the propagation loss in the external cavity. If the passive external cavity has no propagation loss, the intrinsic linewidth of the laser will decrease endlessly. But when the passive external cavity has a certain propagation loss, the intrinsic linewidth of the laser will gradually converge as the physical length of the external cavity increases. Light continues to lose energy in a lossy extended cavity until its energy is substantially lost, at which point there is no longer any benefit from increasing the external cavity length. Due to the different propagation loss in the external cavity, the cavity length is also different when the intrinsic linewidth converges.

In general, increasing the length of the passive external cavity is very effective in reducing the intrinsic linewidth of the semiconductor laser, but the propagation loss of the cavity ultimately determines the effectiveness of this method. It is also consistent with the simulation results presented in [Paper D], where the intrinsic linewidth of the OPO signal decreases as the feedback waveguide length increases. At the same time, the intrinsic linewidth is also influenced by the feedback strength, which is in turn partially determined by the propagation loss of the waveguide. Excessive waveguide loss leads to weak feedback and a diminished external-cavity effect, resulting in limited suppression of the intrinsic linewidth.

3.3 Microring-based external cavity

If the external mirror is a Bragg grating or multi-rings, as shown in Fig. 3.3, the reflectivity will be frequency-dependent. Here, in the above case, $|r_{\text{eff}}|$ is frequency-independent, so $B = 0$. By adding the frequency selective mirror, B is increased at certain wavelengths, so the intrinsic linewidth is further suppressed.

The calculation of r_{eff} depends on the designs of the external cavities. In the case shown in Fig. 3.3, r_{eff} is expressed as

$$r_{\text{eff}}(\omega) = t_2^2 \cdot t_{\text{passive}}(\omega)^2 \cdot t_{\text{ring1}}(\omega)^2 \cdot t_{\text{ring2}}^2(\omega) \cdot r_3, \tag{3.8}$$

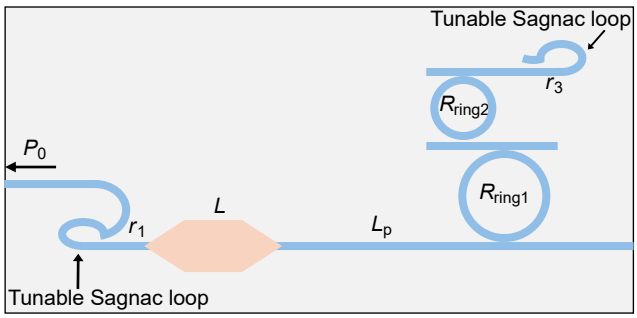

Figure 3.3: Schematic of an on-chip external cavity semiconductor laser based on multi-rings. The polygon with length L represents the active part, and the blue structures represent the passive part. The two mirrors are tunable Sagnac loops, and the reflection coefficients r_1, r_3 can be adjusted by thermal methods using metal microheaters. The waveguide connecting the active part and ring1 can also be heated to change the phase shift, and its length is L_p. The lengths of the two Sagnac rings are negligible. The radii of the two microrings are R_{ring1} and R_{ring2}, respectively, where R_{ring1} is slightly larger than R_{ring2}.

where t_2 is the coupling between the active waveguide with the passive waveguide. t_{passive}, t_{ring1}, t_{ring2} are the electric field transmission coefficients of the passive phase shifter with the length of L_p, the two microrings.

At the same time, the effective cavity length L_{eff} can also be obtained by calculating the time delay of the entire external cavity. Because the time delay is calculated based on the round-trip time, half the round-trip time should be used when calculating the effective cavity length.

$$L_{\text{eff}}(\omega) = \frac{d\varphi_{\text{eff}}(\omega)}{d\omega} \cdot \frac{v_{\text{g,passive}}}{2}. \tag{3.9}$$

Based on the above equations, the external effective reflectivity r_{eff}, effective cavity length L_{eff}, coefficients A, B, F and intrinsic linewidth $\Delta\nu$ are calculated as shown in Fig. 3.4. Because the effective reflectivity r_{eff} of the external cavity is wavelength selective, the external reflector has strong reflection only at the resonant wavelength shared by the two microrings, which means that the loss of the external cavity is low at the wavelength. The two microrings have slightly different sizes, so the FSR caused by the Vernier effect is quite large. This undoubtedly filters the original broadband active gain again in the wavelength selection of the entire cavity. Similar to r_{eff}, the effective length L_{eff} is also symmetric with the common resonant wavelength and is maximum at the wave-

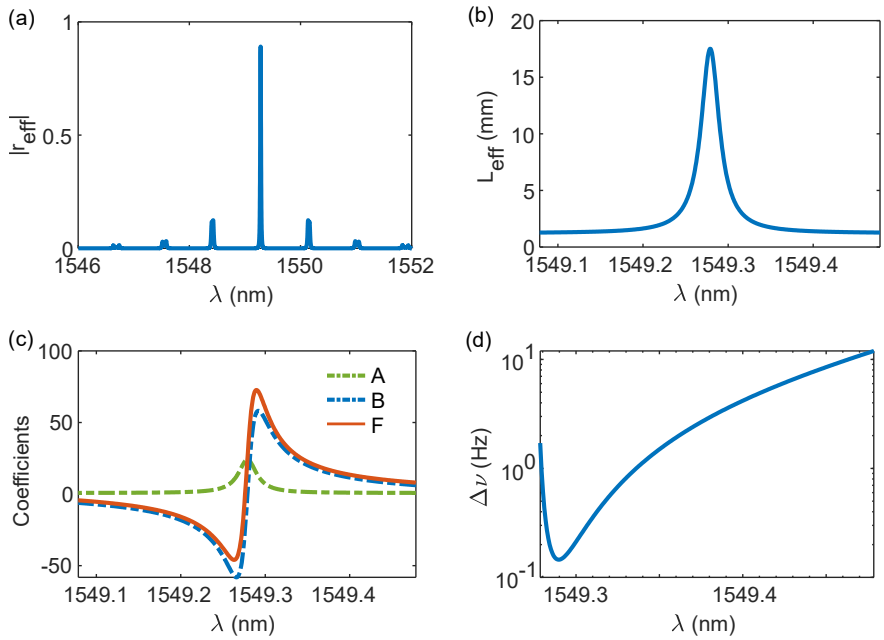

Figure 3.4: (a) Magnitude of the effective reflectivity r_{eff}. (b) Effective length L_{eff} of the external cavity. (c) Coefficients A, B, F. (d) Theoretically estimated intrinsic linewidth $\Delta\nu$. They are all related to the laser wavelength λ. Parameters used in the simulation: $\alpha = 5$, $n_{\text{sp}} = 2$, output power $P_0 = 1$ mW, lengths of active, passive parts $L = 0.7$ mm, $L_p = 1$ mm, group index $n_{\text{g,active}} = 3.6$, $n_{\text{g,passive}} = 2$, reflection coefficients $r_1 = 0.9$, $r_3 = 1$, propagation losses of active, passive parts $\alpha_c = 13$ cm^{-1}, $\alpha_p = 2$ dB/m, the coupling coefficient between microrings with bus waveguides $\kappa = 0.09$, radii of two microrings $R_{\text{ring1}} = 250$ μm, $R_{\text{ring2}} = 240$ μm. Coupling loss between the active part with the passive part is 0.5 dB, so $t_2 = 10^{(-0.5/20)}$.

length, which is much longer than the physical length of the external cavity.

In addition, since the effective length of the external cavity is maximum at the common resonant wavelength, the factor A is maximum at the same location. The factor B is proportional to $d\ln|r_{\text{eff}}(\omega)|/d\omega = d(\alpha_p L_{\text{eff}})/d\omega$, which corresponds to the derivative of the effective length L_{eff} with respect to frequency [79, 82, 139], so it is centrally symmetric and its maximum is located at longer wavelength than the common resonance. Under the combined effect of A and B, the maximum F is also located on the long wavelength side of the resonant wavelength, and the optimal intrinsic linewidth can be obtained at the maximum F point.

In other words, the linewidth suppression induced by effective mirror feedback can theoretically perform better when the laser wavelength is slightly increased relative to the common resonant wavelength.

Compared with long-waveguide based external cavities, the microring based external cavity is more complicated when calculating the effective reflectivity r_{eff}. On the one hand, the microring provides further wavelength selection for the external cavity, but its L_{eff} is similar to the waveguide length L_p in the long-waveguide based external cavity. The lower the propagation loss or the longer the L_{eff}, the better the suppression effect on the intrinsic linewidth. It's just that the L_{eff} of the microring based external cavity is wavelength selective. At non-resonant wavelengths, the microrings are wasted because they are not utilized. At the resonant wavelength, the equivalent length brought by the microrings is longer than the physical length, and the suppression of the intrinsic linewidth is stronger. On the other hand, due to the wavelength selectivity of the microring, the factor B is non-zero, so it can provide additional suppression effect at certain wavelengths. Because of its wavelength selectivity, the operating frequency and phase shifter need to be finely adjusted during design or experiment.

Chapter 4

Self-injection locking technique

In the previous chapter, the intrinsic linewidth of optical coherent oscillators are investigated through theoretical analysis and numerical simulations, with particular emphasis on the critical roles of the external cavity length and optical loss. These results demonstrated that external-cavity feedback can effectively suppress the intrinsic linewidth, provided that sufficient feedback strength is maintained. This chapter introduces an alternative linewidth suppression technique – self-injection locking. This method exploits resonant optical feedback to stabilize the oscillator frequency and reduce phase noise. Both the theoretical principles and the experimental implementation of self-injection locking are discussed in detail, providing a comprehensive understanding of its effectiveness and practical applicability for realizing narrow-linewidth optical sources.

4.1 Dynamics of self-injection locked lasers

For the semiconductor laser with the external cavity, the passive and active parts can be considered as a whole. The reflectors at both ends can be designed on the passive platform, and the active part is mainly responsible for providing optical gain. The lasing frequency is determined by the two parts. Without the passive part, the laser would have an extremely low Q factor, or even not be a laser due to the lack of reflectors built into the passive part. When a semiconductor laser is self-injection locked, the external feedback is mainly provided by the backscattering which is very weak [140–143]. The generated frequency is mainly de-

termined by the semiconductor laser itself. Even without the external feedback, the laser still operates normally, just with higher phase noise. When the semiconductor laser is self-injection locked to the external resonator by aligning their resonant frequencies, the generated frequency is determined by the resonator. It can only be fine-tuned within a narrow wavelength range, otherwise the self-injection locking will be interrupted due to the large frequency difference of the two components.

4.1.1 Laser dynamics

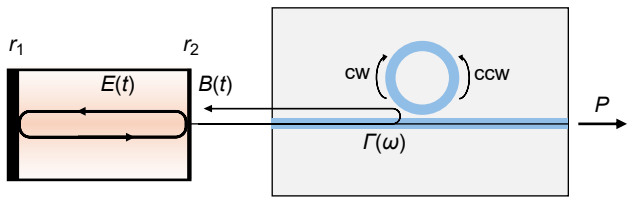

Figure 4.1: Schematic of a self-injection locked semiconductor laser. The reflectivities of the mirrors on both sides of the laser are r_1, r_2, and the electric field is $E(t)$. The laser is incident from the left side of the microring resonator and output from the right side. There are two modes in the microring resonator, one propagating in clockwise (cw) and the other propagating in counterclockwise (ccw), and they are coupled to each other. The electric field reflected by the microring is $B(t)$, and the reflection coefficient is $\Gamma(\omega)$.

The self-injection locking system is shown in Fig. 4.1. The laser operates at a single frequency and the instantaneous electric field $E(t) = |E(t)|\exp(j\phi)$ is reflected from the output mirror with the reflection coefficient of r_2. $E(t)$ is the sum of the electric field reflected from both mirrors and the electric field transmitted back to the laser cavity due to the backscattering in the microring resonator [144]. The backscattering is introduced by the inhomogeneity of the waveguide interface [145]. So the electric field in the laser cavity can be expressed as

$$\begin{aligned}|E(t)|\exp[j\phi(t)] = {} & jt_2B(t) \\ & + r_1r_2\,|E(t-\tau_0)|\exp[j\omega\tau_0 + j\phi(t-\tau_0) + (g-\alpha_c)L],\end{aligned} \tag{4.1}$$

where $t_2 = \sqrt{1-r_2^2}$ is the transmission coefficient, τ_0 is the round-trip time of the FP laser cavity, g is the gain coefficient, α_c is the propagation loss of the active medium, L is the laser cavity length, ω is the

instantaneous angular frequency of the generated light, ω_d is the resonant angular frequency of the FP laser cavity. In the self-injection locking state, the frequency finally generated by the system may not be equal to the resonant frequency of the FP laser cavity, so ω is used instead of ω_d.

Similarly, the reflected electric field $B(t)$ is

$$B(t) = \frac{jt_2\Gamma(\omega)}{r_2}|E(t-\tau_s)|\exp[j\omega\tau_s + j\phi(t-\tau_s)], \tag{4.2}$$

where τ_s is the round-trip time from laser coupling to the microring resonator, and $\Gamma(\omega)$ is the frequency-dependent reflection coefficient of the microring resonator. If the resonant angular frequency of the microring resonator is ω_m, combined with the steady-state expression [144],

$$\Gamma(\omega) = -\frac{j\eta\kappa_m^2\gamma/2}{(\kappa_m/2 - j(\omega-\omega_m))^2 + (\kappa_m\gamma/2)^2}, \tag{4.3}$$

where $\kappa_m = \kappa_{mi} + \kappa_{mc}$ is the total decay rate of the microring resonator, κ_{mi}, κ_{mc} are the intrinsic, extrinsic decay rate. $\eta = \kappa_{mc}/\kappa_m$, and γ is mode-splitting coefficient related to the mutual coupling between the cw and ccw modes.

By taking the time-independent solutions (steady-state) for $E(t)$, $\phi(t)$ [143], and introducing the detuning of the laser cavity frequency from the microring resonant frequency $\xi = 2(\omega_d - \omega_m)/\kappa_m$, as well as the generation detuning of the generated frequency from the microring resonant frequency $\zeta = 2(\omega - \omega_m)/\kappa_m$, their relationship is as follows

$$\xi = \zeta + \frac{K}{2}\frac{2\zeta\cos\psi + (1+\gamma^2-\zeta^2)\sin\psi}{(1+\gamma^2-\zeta^2)^2 + 4\zeta^2}, \tag{4.4}$$

where $\psi = \omega\tau_s - \arctan\alpha + 3/2\pi$ is the phase delay (α is also linewidth enhancement factor). K is the combined coupling coefficient [144]. This relationship is usually called tuning curve as shown in Fig. 4.2.

For a free-running laser, the tuning curve is linear with a slope of unity, as indicated by the blue dashed line, meaning that the output wavelength directly follows the resonant frequency of the laser cavity. In contrast, a self-injection-locked laser exhibits a tuning curve with an extended nearly horizontal region (from point III to point iii), which corresponds to the locking regime.

As the laser cavity frequency ω_d is tuned from lower to higher values and gradually approaches the microring resonant frequency ω_m, the

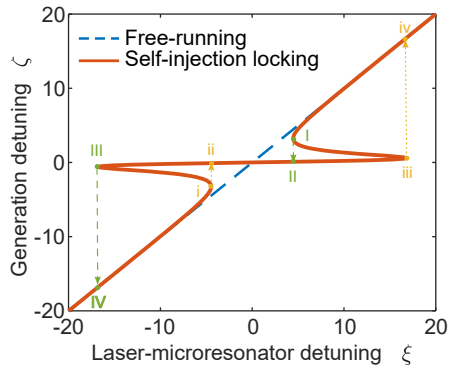

Figure 4.2: Tuning curve of a semiconductor laser locked to a microring resonator. The horizontal axis represents the difference between the laser resonant frequency and the microring resonant frequency, and the vertical axis represents the difference between the system output frequency and the microring resonant frequency.

generated frequency ω initially follows a line similar to that of the free-running laser. This behavior continues until the first inflection point (point i) is reached. At this point, the system abruptly transitions into the low-slope region (point ii), indicating the onset of self-injection locking. Within this regime, changes in the laser cavity frequency have little influence on the generated frequency, which remains effectively fixed.

As tuning continues, the system remains locked until the second inflection point (point iii) is encountered, beyond which the locking condition is lost and the generated frequency resumes following the laser cavity frequency. In the locked region, the generated frequency is primarily determined by the microring resonance rather than by the laser cavity itself, which is known as frequency pulling. A similar behavior is observed when the laser frequency is swept in the opposite direction. The frequency range over which the slope remains nearly flat defines the locking bandwidth.

4.1.2 Linewidth reduction

The intrinsic linewidth reduction can also be seen from the tuning curve. After simplifying and differentiating Eq. 4.4, the linewidths of the free-running laser and the self-injection locked laser can be approximately

expressed as [144]

$$\frac{\Delta\nu_{\text{locked}}}{\Delta\nu_{\text{free}}} = \frac{d\omega}{d\omega_d} = \frac{d\zeta}{d\xi} = \frac{Q_d^2}{Q_m^2}\frac{1}{16\Gamma_m^2(1+\alpha^2)}, \tag{4.5}$$

where Q_d, Q_m are the total Q factors (ratio of resonant frequency to decay rate) of the FP laser cavity and the microring resonator, α is the linewidth enhancement factor. $\Gamma_m = \Gamma(\omega = \omega_m)$, which is the reflection coefficient calculated by Eq. 4.3. In general, the Q factor of a laser cavity is much lower than that of a low-loss microring resonator. Because of this disparity, when a laser is self-injection locked to a high-Q microring, the slope $d\zeta/d\xi$ in the nearly flat region of the tuning curve becomes extremely small. Physically, this means that even if the laser cavity frequency fluctuates, the corresponding change in the generated frequency is strongly suppressed by the high-Q resonator [146, 147]. As a result, the frequency noise of the self-injection-locked laser is greatly reduced compared to a free-running laser. This reduction in frequency fluctuations directly translates into a significant narrowing of the intrinsic linewidth, demonstrating why self-injection locking is an effective technique for achieving ultra-stable, narrow-linewidth laser operation.

[Paper C] demonstrates a self-injection locking scheme that is conceptually similar to the approach discussed here. However, the optical source in that study is a soliton microcomb rather than a semiconductor laser, and the external resonator is implemented using a fiber-loop cavity. Owing to its long optical path length and low propagation loss, the fiber-loop cavity exhibits a Q factor that is significantly higher than that of a Si_3N_4 microring resonator. In the reported scheme, a comb line is spectrally filtered, then injected into the fiber-loop cavity and subsequently fed back into the Si_3N_4 microring which is used to generated soliton microcomb. As a result of the high Q external feedback provided by the fiber loop, the intrinsic linewidth of the selected frequency component is substantially suppressed. In addition, the longer external cavity contributes to decrease the TRN contribution to the linewidth.

4.2 Experimental study on self-injection locked lasers

On the integrated Si_3N_4 platform, self-injection locking is typically realized by locking a semiconductor laser to a high-Q Si_3N_4 microring, thereby suppressing the laser linewidth [77, 86, 148, 149]. The following

section describes how linewidth reduction can be achieved experimentally using self-injection locking.

4.2.1 Experimental procedures

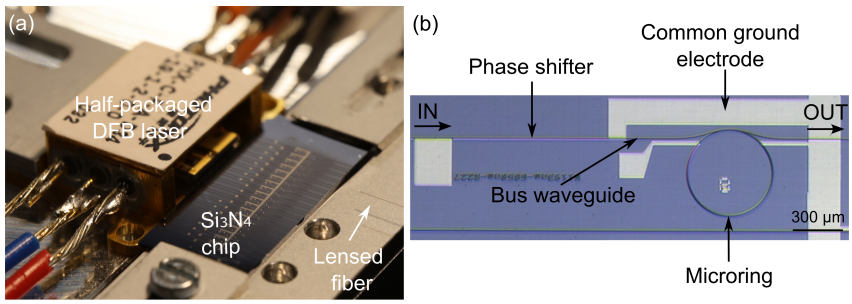

Figure 4.3: (a) Photo of the experimental setup for self-injection locking. The DFB laser on the left is butt-coupled to the Si_3N_4 chip in the middle, and the light is then collected by the lensed fiber on the right. (b) Microscope image of a typical Si_3N_4 device. The DFB laser can be locked to the microring resonator.

The experimental setup of a self-injection locked semiconductor laser is shown in Fig. 4.3(a). The half-packaged DFB laser has two pins for drive current and four pins for temperature control. The highest output optical power is around 80 mW at the driving current of 300 mA. The operating wavelength is around 1550 nm, and the tunable wavelength range is about 2.4 nm. The operating wavelength can be tuned by changing the driving current or temperature of the laser. The former allows for more precise wavelength adjustment.

Fig. 4.3(b) shows a 740 nm thick Si_3N_4 microring resonators, with 3 μm thick cladding layers on both the upper and lower sides. Two metal microheaters are integrated on the device. One is on microring resonator, the other is on a section of the bus waveguide, which also serves as a phase shifter. The two microheaters has a common ground electrode.

With the experimental platform established, the self-injection locking process can be carried out through the following procedures. This experiment could be divided into four main steps: optical coupling alignment, coarse frequency alignment, phase optimization, and fine frequency alignment.

Optical coupling alignment

The laser chip is extended about 1 mm outside its package to facilitate optical coupling with the Si_3N_4 chip. The laser emits a mode with a spot diameter of approximately 2.8 μm, slightly larger than the 2.5 μm mode diameter of a lensed fiber we usually use.

Since no optical isolator is placed between the laser and the chip, any light reflected or scattered back from the chip can enter the laser cavity and affect its operation. To prevent direct reflections from the Si_3N_4 facet from interfering with the laser, the chip is slightly tilted relative to the laser axis. For precise alignment, the stage holding the DFB laser is equipped with a six-axis adjustment system, allowing fine control over position and angle in all directions. This configuration ensures efficient coupling while minimizing unwanted back-reflections that could destabilize the laser.

Because the on-chip microheaters must be electrically connected to probes, the chip is mechanically fixed and cannot be repositioned during the experiment. Consequently, optical coupling is achieved by adjusting the position of the lensed fiber and the DFB laser. In the experiment, the chip is first aligned with the lensed fiber. A red alignment beam is coupled into the lensed fiber to achieve coarse positioning. When the red light is visibly coupled into the bus waveguide, coarse alignment is considered complete. The red alignment beam is then disconnected, and the lensed fiber is connected to a power meter. The position of the DFB laser is coarsely adjusted to maximize the optical power received by the power meter. Finally, fine adjustments are performed separately on the lensed fiber and the DFB laser to further maximize the output power.

Coarse frequency alignment

Once the laser is successfully coupled to the Si_3N_4 chip, the next step for achieving self-injection locking is to align the resonant frequency of the microring with the laser emission frequency. This alignment ensures that light from the laser can efficiently couple into the microring and be fed back into the laser cavity, enabling linewidth suppression. There are three common approaches to achieve this frequency alignment: adjusting the laser drive current, tuning the laser operation temperature, or changing the temperature of the microring. In our experiments, we often adjust the microring temperature. This approach has the advantage of not altering the parameters of the laser, making it easier to monitor the

coupling condition.

Alignment can be determined by observing the output power of the microring. When the laser frequency matches the microring resonance, a part of the light is coupled into the microring, causing the transmitted output power to drop. At this stage, only a coarse adjustment of the microring temperature is needed to bring the two resonances into approximate alignment, preparing the system for fine tuning and stable self-injection locking.

Phase optimization

According to Eq. 4.2, the round-trip time of the light in the laser and the microring directly affects the optical feedback. Therefore, to achieve stable self-injection locking, it is crucial to carefully adjust the phase shift between the laser and the microring. Building on the coarse alignment achieved in the previous step, we finely tune this phase by sweeping the temperature of the microring and monitoring the resonance waveform on an oscilloscope, as illustrated in Fig. 4.4.

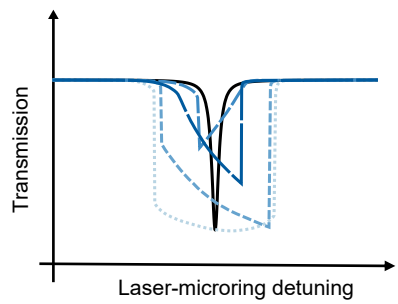

Figure 4.4: Schematic illustration of the transmission response of the Si_3N_4 microring resonator. The detuning between the laser and the microring resonance can be adjusted either by tuning the laser frequency or by changing the microring temperature. The black curve shows the resonance measured using a commercial laser. The blue curves correspond to the resonances obtained with the DFB laser, where the curve intensity represents the phase shift between the DFB laser and the microring. The illustrated phase shifts are 0, $\pi/2$, π, and $3\pi/2$, respectively.

When a commercial laser is used as the input source, which does not allow any feedback to re-enter the laser cavity, the microring resonance exhibits a Lorentzian profile, as shown by the black curve. In contrast, when using a DFB laser without an isolator, the feedback modifies the

resonance shape, which depends sensitively on the phase shift between the DFB laser and the microring resonator. If the phase is not properly adjusted, the resonance appears narrow and shallow [144, 150]. Tuning the phase can be achieved experimentally by adjusting the temperature of the waveguide connecting the DFB laser and the microring.

As the phase shift approaches the optimal value, the resonance gradually broadens and eventually adopts a characteristic "U" shape. This flattened or widened resonance indicates that, near the microring resonant wavelength, the DFB laser is effectively locked to the microring. In this locked regime, the output frequency of the system is determined primarily by the microring resonance rather than the laser cavity, in agreement with the frequency pulling discussed in the theoretical analysis of the previous section.

Fine frequency alignment

After optimizing the phase shift, the microring temperature scan should be stopped, and the temperature is finely adjusted to bring the microring resonance back into precise alignment with the DFB laser frequency. When the output power as low as possible, indicating that the laser is aligned with the microring's resonant frequency, the DFB laser enters the self-injection locked state. Finally, complete the locking process and measure the linewidth of the self-injection locked laser.

4.2.2 Experimental results

As shown in Fig. 4.5(a), the beating spectrum of the DFB laser is relatively broad before self-injection locking. However, once the laser is locked to a Si_3N_4 microring resonator with an FSR of 100 GHz and an intrinsic Q factor of ∼15 million, the beating spectrum narrows dramatically, indicating a significant reduction in frequency fluctuations. This effect is further quantified in the frequency noise PSDs shown in Fig. 4.5(b). For the free-running DFB laser, the intrinsic linewidth is approximately 77 kHz. After self-injection locking to the microring, the intrinsic linewidth drops to just 103 Hz, which is comparable to or even slightly better than that of a commercial TOPTICA (CTL 1550) laser. Locking to a 20.5 GHz microring with an intrinsic Q factor of ∼17 million, further narrows the linewidth, reducing it to just 9 Hz. This demonstrates that self-injection locking with high Q microrings can drastically suppress the intrinsic linewidth, highlighting the effectiveness

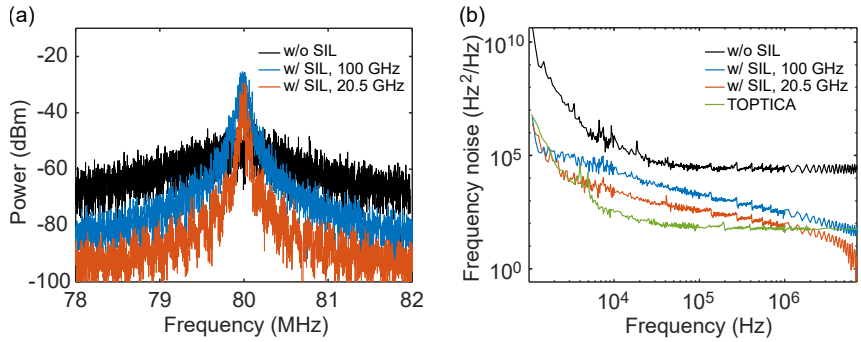

Figure 4.5: (a) Beating spectrum from the self-heterodyne measurement. The frequency shift introduced by the AOM is 80 MHz. (b) Measured single-sided frequency noise PSDs of the DFB laser. The black curve represents the PSD of the free-running laser (w/o SIL). The blue and orange curves correspond to the laser locked (w/ SIL) to 100 GHz and 20.5 GHz microring resonators, respectively. The green curve shows the PSD of a TOPTICA laser.

of this technique for generating ultra-narrow linewidth integrated lasers.

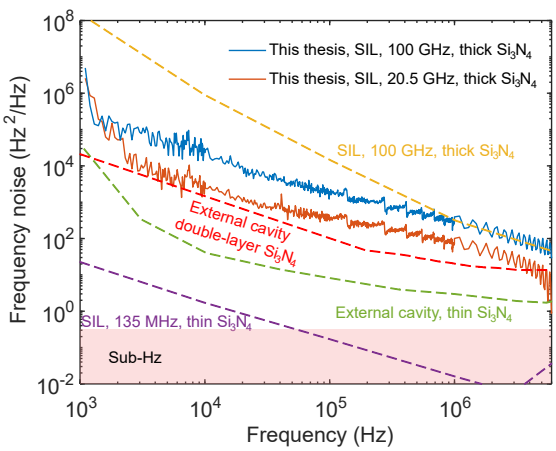

Figure 4.6: Comparison with previously reported results, including our work, two self-injection-locked semiconductor lasers from other groups [77, 84], and two external-cavity laser implementations [77, 151], all demonstrated on silicon nitride platforms. The shaded region represents an intrinsic linewidth in the sub-hertz regime.

As shown in Fig. 4.6, we compare our results with previously reported self-injection-locked semiconductor lasers [77, 84]. For thick Si_3N_4 platforms, our device achieves a comparable noise level at high offset

frequencies and demonstrates better performance at low offset frequencies [84]. In contrast, devices based on thin Si_3N_4 exhibit significantly better overall performance. Thin Si_3N_4 platforms can support ultra-low loss microresonators with Q factors reaching several hundred million. In addition, their larger mode volumes help reduce the impact of thermorefractive noise. The combination of the two advantages leads to ultra-narrow linewith as low as sub-Hz [77].

If external cavity semiconductor lasers are also taken into consideration [75, 151], the overall linewidth reduction is generally not as strong as that achieved by self-injection locking, but their main advantage lies in enabling wide continuous tuning, typically at least several tens of nanometers while maintaining single mode operation. Self-injection locking feeds the weak backscattered light from the microresonator back into the laser cavity. The locking can only be achieved when the frequency of the feedback light matches the resonance frequency of the laser cavity and the phase condition is satisfied, thereby leading to linewidth narrowing. Once locked, the laser frequency is predominantly determined by the microresonator. Therefore, wide-range tuning requires simultaneous tuning of both the microresonator and the laser.

Chapter 5

Ultra-low loss silicon nitride waveguides

The preceding chapters presented a detailed discussion of the theory of intrinsic linewidth and the methods for suppressing the intrinsic linewidth of optical coherent oscillators. We demonstrated that the achievable linewidth reduction depends critically on both the propagation loss of the passive photonic platform and the length of the external cavity. This chapter provides an overview of waveguide propagation losses, the fabrication processes of ultra-low loss silicon nitride waveguides, and the key considerations involved in manufacturing long waveguides.

5.1 Waveguide losses

Taking the microring shown in Fig. 5.1 as an example, waveguide losses can be categorized into four main mechanisms. Absorption loss mainly originates from the intrinsic properties of the material and surface absorption introduced by defect bonds or dangling bonds after etching [63,152,153]. Bending loss occurs when the waveguide bending radius becomes sufficiently small, leading to mode leakage. Scattering loss is caused by sidewall and surface roughness or film defects, while radiation loss arises from particles or other structures located near the waveguide [154–157]. Unlike absorption loss which is converted into heat, the latter three mechanisms typically convert guided modes into unconfined modes, which then dissipate into the surrounding environment [63].

Attention to material processing, device designing and fabrication

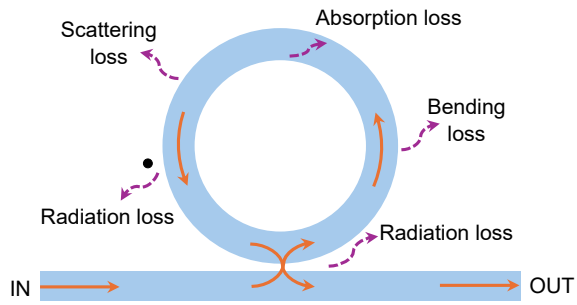

Figure 5.1: Schematic of waveguide losses. The orange solid arrows represent the propagation of the fundamental mode (TE_0), and the purple dashed arrows illustrate the various loss mechanisms that attenuate the guided optical field. The small black dot represents a particle close to the microring.

environment is essential for achieving low-loss, high-performance Si_3N_4 waveguides.

Absorption loss

For Si_3N_4 films deposited using low-pressure chemical vapor deposition (LPCVD), high-temperature annealing plays a crucial role in improving optical performance. This process effectively breaks N–H bonds within the film, which eliminates the absorption peak that typically appears near 1520 nm [158, 159], thereby reducing propagation loss in that wavelength region. Surface absorption caused by dangling bonds can be compensated by introducing an additional blanket layer, as demonstrated in [Paper A]. The thin layer passivates the dangling bonds at the surface, thereby reducing absorption loss [63].

Bending loss

Bending can break the axial symmetry of the waveguide, causing the mode to no longer be tightly confined at the center of the waveguide but instead to shift toward the side of the bend, see the inset of Fig. 5.2. This occurs because the optical path length is longer on the outer side. To maintain a constant phase front, light must propagate faster along the outer edge, resulting in a redistribution of energy. When the bending radius becomes too small, part of the optical energy radiates outward, leading to bending loss. As shown in Fig. 5.2, the bending loss decreases with increasing bending radius. Therefore, bending loss can be mitigated

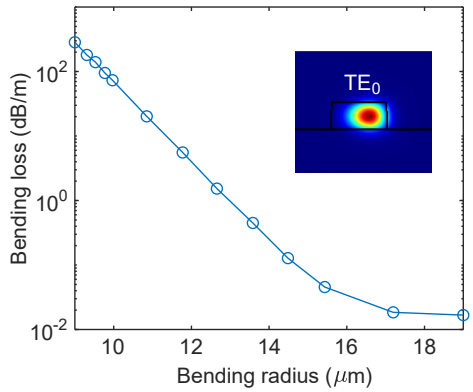

Figure 5.2: Relationship between the bending loss of the fundamental TE mode and the bending radius. The waveguides have a cross-sectional size of 1600×660 nm^2 with a sidewall angle of 87°.

by increasing the waveguide bending radius, which helps maintain strong optical mode confinement and prevents light from radiating out of the waveguide.

Radiation loss

Additionally, during fabrication, the cleanliness of the chip surface must be carefully controlled. Even small residual particles or contaminants near the waveguides can perturb the optical mode and induce scattering, significantly increasing radiation loss. In addition to avoiding particles or contaminants, sufficient spacing should be maintained between unrelated waveguides to prevent unintended coupling and additional radiation loss. In cases where close coupling is required, such as between a microring resonator and a bus waveguide, special design strategies can be employed to minimize radiation loss while preserving coupling efficiency. One such approach is the use of a racetrack-shaped microring, which enhances the coupling efficiency by increasing the interaction length between the microring and the bus waveguide rather than by reducing the gap width [60].

In addition, as demonstrated in [Paper B], achieving high conversion efficiency and output power in optical parametric oscillators requires the gap between the bus waveguide and the microring resonator to be as small as possible in order to enhance coupling. However, the close proximity of the bus waveguide also introduces additional radiation loss to

the microring and enhances the conversion to higher order modes. In this configuration, a clear Vernier effect arises between the fundamental mode and higher-order modes supported by the microring. At certain discrete wavelengths, this modal interaction gives rise to a bound states in the continuum, which significantly suppresses radiation loss in the microring waveguide [102]. Although the radiation loss induced by the bus waveguide can be reduced through this mechanism, the overall propagation loss of the Si_3N_4 microring remains primarily limited by scattering associated with sidewall roughness.

Scattering loss

Surface roughness in waveguides can be effectively reduced by carefully optimizing the thin-film deposition process or by employing post-deposition polishing techniques, which help create a smoother top surface and minimize scattering losses [156]. Sidewall roughness, however, arises primarily during the lithography and etching steps and requires a different mitigation approach. This can be addressed by optimizing the lithography exposure parameters and the etching recipes to produce smoother sidewalls. Furthermore, by depositing an ultra-thin Si_3N_4 blanket layer demonstrated in [Paper A], sidewall roughness can be also reduced. This post-etch deposition can smooth the waveguide sidewalls, effectively reducing microscopic irregularities and thereby lowering scattering loss.

If waveguide roughness cannot be further optimized due to equipment limitations, scattering loss induced by roughness can instead be reduced by increasing the waveguide cross-sectional dimensions. As shown in Fig. 5.3, when the Si_3N_4 waveguide width is increased from 800 nm to 2.5 μm, the propagation loss is reduced by more than an order of magnitude, with the minimum loss approaching 1.4 dB/m. This reduction occurs because the fundamental TE mode becomes more strongly confined to the central region of the waveguide. As the waveguide width increases, the optical field intensity at the sidewalls decreases, thereby weakening the interaction between the guided mode and sidewall roughness and reducing scattering-induced propagation loss [160]. Owing to its simplicity and effectiveness, this approach is widely adopted in low-loss photonic applications, where multimode waveguides are not a concern.

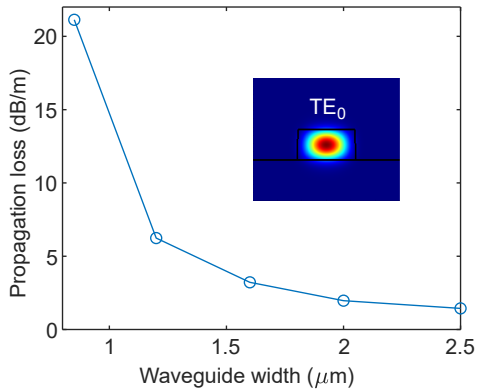

Figure 5.3: Relationship between the propagation loss of the fundamental TE mode and the waveguide width. The thickness of waveguides is 740 nm. Measurements are performed over the wavelength range from 1560 to 1620 nm, which avoids the absorption peak of LPCVD Si_3N_4. The reported propagation loss is the mean of statistical data from 36 samples measured at different wavelengths on the same chip.

5.2 Overview of process flow

The entire fabrication process follows a subtractive approach [68, 159]. And the detailed fabrication process for low-loss Si_3N_4 waveguides is illustrated in Fig. 5.4, where each step plays a critical role in achieving low propagation loss.

5.2.1 Wafer preparation

The process begins with thermally oxidized 4-inch silicon wafers, which serve as the substrate and lower cladding, as shown in step (I). The entire wafer is ~525 μm thick, and the thermally oxidized layer is ~3 μm thick.

Since Si_3N_4 films exhibit high stress when grown thick directly on the substrate, the films are prone to cracking [161]. Crack barriers are required to stop film cracking during deposition and subsequent thermal processing [162, 163]. Cracks tend to propagate inward from the wafer edges, while the crack barriers effectively prevent their extension, thereby preserving the largest possible central region of a wafer [164–166], as shown in Fig. 5.5(a). These crack barriers are defined using standard photolithography followed by wet etching, as shown in step (II) and (III). The trench patterns shown in Fig. 5.5(b) for the crack barriers are identical, enabling the use of a mask aligner for pattern exposure.

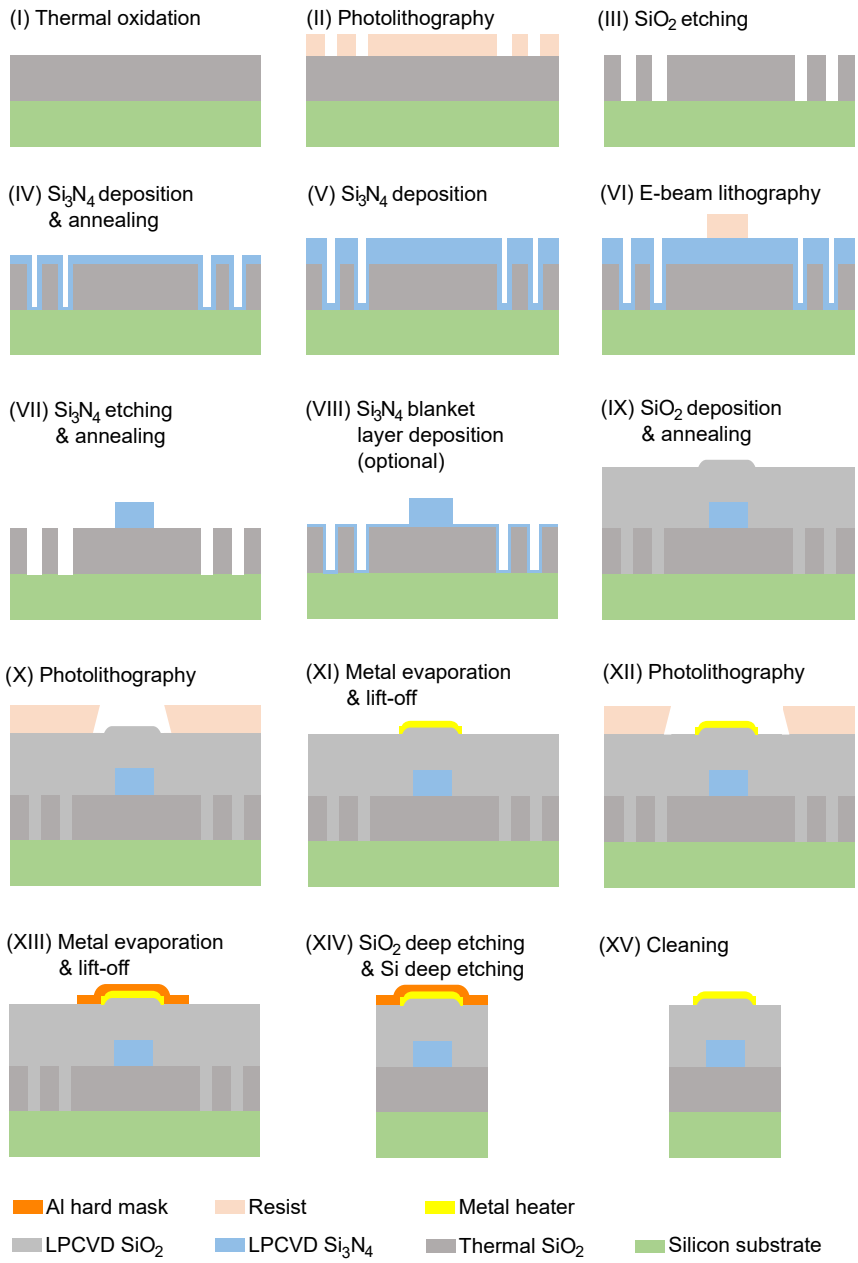

Figure 5.4: Process flow for the fabrication of low-loss thick Si_3N_4 waveguides with integrated metal microheaters. Step (VIII) is optional and is included only for an additional blanket layer deposition, if needed.

After lithography, the patterns are transferred into the thermal SiO_2 layer through wet etching, forming the crack barrier structures. Here, the SiO_2 layer is fully etched.

5.2.2 Waveguide patterning

Following standard wafer cleaning procedures to ensure a contaminant-free surface, a Si_3N_4 film is deposited onto the SiO_2 cladding layer using LPCVD, as shown in step (IV) and (V). The precursor gases dichlorosilane (SiH_2Cl_2) and ammonia (NH_3) react at 770 °C under 250 mTorr to form Si_3N_4 films. The film growth rate is ∼3.5 nm/min. The film thickness decreases from the outer region toward the center, with a uniformity of ∼2%.

Typically, when the Si_3N_4 layer reaches a thickness of approximately 400 nm, high temperature annealing is performed at 1100 °C in a nitrogen (N_2) atmosphere for 3 hours to relieve the intrinsic stress of the thick film and to dissociate N–H bonds introduced during the LPCVD process [158, 159]. After annealing, a second Si_3N_4 layer is deposited using the same LPCVD conditions to obtain the target film thickness required for the subsequent waveguide fabrication.

After deposition of the thick Si_3N_4 film, electron-beam lithography (EBL) is used to define the waveguide patterns, which are subsequently transferred into the Si_3N_4 layer through dry etching, as shown in step (VI) and (VII).

EBL enables precise control over pattern dimensions and placement, making it suitable for the fabrication of high-resolution photonic and electronic devices. First, a layer of electron-beam resist (MaN 2405) is coated onto the wafer surface. A focused electron beam then exposes the resist to define the desired micro- and nano-scale patterns. The beam step size determines how accurate the patterns are. A smaller beam step size improves pattern accuracy and results in smoother sidewalls, but it also increases the exposure time. After weighing the trade-off, a beam step size of 2 nm is used. In addition, the EBL system may have some imperfections, including system noise, environmental noise, and electron beam instability. These effects can be mitigated by implementing a multi-pass exposure strategy [167]. Considering the exposure time, the resist is typically exposed twice to reduce sidewall roughness.

After exposure, the exposed areas of the resist are removed through a development process, thereby forming the patterns which are used for etching. During this etching step, the unprotected regions of the Si_3N_4

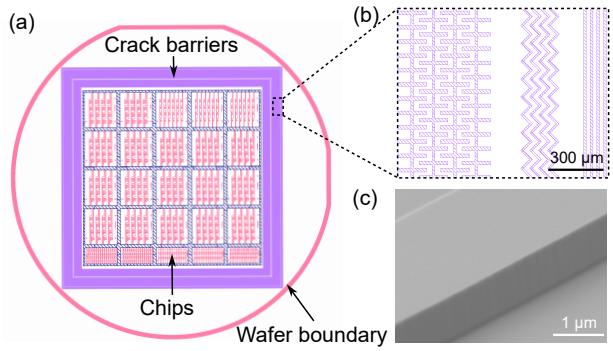

Figure 5.5: (a) GDS layout of a 4-inch wafer with two flats. 25 chips are designed within the region protected by crack barriers, each surrounded by 1 mm wide trenches to facilitate subsequent etching for chip release. (b) Segment of crack barriers. (c) SEM image of a Si_3N_4 waveguide.

film are removed by CHF_3 and O_2 gases, as they are not covered by the negative resist. After removing the remaining resist using a standard cleaning process, the Si_3N_4 waveguides can be checked under a scanning electron microscope (SEM). Fig. 5.5(c) presents an etched Si_3N_4 waveguide, in which line roughness along the sidewall is clearly observable.

Following waveguide etching, a second high-temperature annealing step is performed to further dissociate residual N–H bonds. In this step, the wafers are annealed at 1190 °C in argon (Ar) atmosphere. In [Paper A], an additional blanket layer, shown in step (VIII), is deposited to further reduce the propagation loss of the waveguides. The deposition follows the same recipe as that used for the previous Si_3N_4 films.

5.2.3 Post-processing

Finally, a ∼3 μm thick SiO_2 upper cladding is deposited in multiple layers via LPCVD like step (IX). LPCVD SiO_2 is deposited at 710 °C under 250 mTorr [66, 168], with each run, growing ∼500 nm thick SiO_2 films. Here, with intermediate annealing steps applied to relieve film stress and promote densification of the deposited oxide. The annealing is also carried out at 1100 °C in N_2 atmosphere. These steps help to uniformly fill the gap between the bus waveguides and microring resonators.

To enhance device tunability, microheaters are integrated onto wafers. The refractive index of Si_3N_4 is temperature-dependent, increasing with temperature, which allows precise control of the optical properties of the waveguides. The microheaters are composed of 5 nm thick

titanium (Ti) and 200 nm thick platinum (Pt). The microheaters are fabricated using standard photolithography followed by a lift-off process, as shown in step (X) and (XI). In experimental configurations where multiple heaters must be controlled simultaneously, the heater contact electrodes are designed such that different heaters share a common ground electrode, while maintaining maximum separation between individual heaters to minimize thermal crosstalk, as shown in [Paper D].

To couple light from lensed fibers into the Si_3N_4 chips, edge couplers are employed [169]. The release of individual chips from wafers requires a multi-step dry etching process, as shown in step (XII)-(XV). First, release trenches are defined using photolithography, and a 300 nm thick aluminum (Al) film is evaporated to serve as a hard mask, which improves etching selectivity and protects the underlying structures during SiO_2 removal [170, 171]. After the SiO_2 cladding is fully etched, deep silicon etching is performed using a separate tool that only allows photoresist as a mask. Therefore, another photolithography step is needed to define the trench patterns for this deep etch. By carefully executing these steps, the silicon substrate is almost completely removed, effectively releasing the Si_3N_4 chips while maintaining the integrity of the waveguides and couplers.

5.3 Considerations for manufacturing long waveguides

Whether implementing a narrow-linewidth semiconductor laser with an external cavity or using the self-injection locking approach, achieving ultra-low propagation loss and maintaining a long feedback loop are both essential. The previous section described the fabrication of low-loss Si_3N_4 waveguides and microrings. Compared with microrings, we need to pay additional attentions to long waveguides because of the longer length and larger footprint. In this section, we focus on the important considerations that must be addressed when fabricating long, low-loss waveguides.

EBL is employed to define Si_3N_4 waveguide patterns. In EBL, the writing field refers to the maximum area that can be exposed by deflecting the electron beam without translating the sample stage. For the exposure system we use, the maximum writing field is 1040×1040 μm^2. When the dimensions of a waveguide exceed a single writing field, multiple adjacent fields must be exposed sequentially. As a result, stitching errors can occur at the interfaces between neighboring writing fields. In

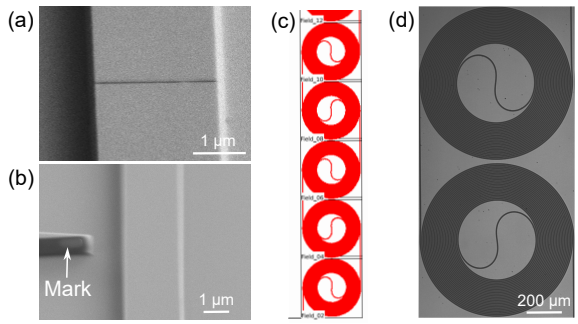

Figure 5.6: (a) SEM image of a long Si_3N_4 waveguide showing a stitching error at the interface between adjacent writing fields. (b) SEM image of a long Si_3N_4 waveguide without stitching error. The mark indicates the boundary between adjacent writing fields. (c) Layout of the writing field arrangement for a long waveguide. The red curve represents the waveguide path, and the black boxes denote individual writing fields. The numbers of writing fields are all even because a double-pass exposure mode is used, and writing fields with odd numbers are covered. (d) Microscope image of two cascaded spiral waveguides.

theory, stitching errors arise from a combination of mechanical inaccuracies in the translation stage, beam distortions at the edges of the writing fields, and variations in wafer height [172]. When a waveguide crosses a writing-field boundary, these stitching errors can lead to discontinuities shown in Fig. 5.6(a), lateral offsets, or angular misalignment of the waveguide segments. The magnitude of such errors can reach several tens of nanometers, which can introduce significant scattering losses and degrade optical performance.

Importantly, stitching errors are not primarily caused by inaccuracies in the motion of the sample stage, as the stage position is monitored and controlled with high precision using a laser interferometer. Instead, these errors mainly arise from imperfect electron-beam deflection and calibration limitations of the deflection system [66]. In addition, variations in wafer height or surface non-flatness can exacerbate beam deflection inaccuracies by changing the effective working distance during exposure. Therefore, the wafer height must be carefully measured and adjusted before exposure to ensure a flat surface, which effectively minimizes stitching errors, improves pattern continuity across writing-field boundaries, and enables the fabrication of waveguides without discontinuities, see Fig. 5.6(b).

The physical dimensions of the microring resonators are typically

much smaller than the maximum writing-field size, and therefore stitching errors at the boundaries between adjacent writing fields can be effectively avoided for these structures. In contrast, the fabrication of meter-long waveguides inevitably requires the pattern to span multiple writing fields, making stitching errors unavoidable.

To mitigate the impact of stitching errors in long waveguides, careful layout design is essential. In addition to minimizing stitching-induced discontinuities, the layout must also reduce the overall footprint, improve structural compactness, and account for spatial nonuniformities in the Si_3N_4 film thickness across the wafer. More importantly, excessive crossings of writing-field boundaries should be avoided whenever possible.

To address these considerations, the long waveguide is designed as a series of cascaded spiral sections. This geometry allows the waveguide to be distributed over a relatively small area while maximizing its total length, thereby reducing the number of writing-field crossings and improving fabrication uniformity. As a result, the adverse effects of stitching errors are minimized, leading to improved waveguide continuity and reduced optical loss. As presented in [Paper D], we designed a waveguide approximately 1.5 m long, composed of 24 spiral units arranged in a 3×8 matrix. This matrix layout allows the long waveguide to be compactly folded, significantly reducing the device footprint while maintaining the required optical path length.

Each spiral waveguide is fully contained within a single writing field, as illustrated in Fig. 5.6(c). The writing fields are exposed sequentially following the optical propagation direction of the waveguide, which ensures continuity of the pattern at the interfaces between adjacent fields. In this work, a multi-pass exposure mode with two passes is employed [173], meaning that each writing field is exposed twice using the same exposure parameters and scanning sequence. As a result, the numbers of writing fields shown in the figure are even numbers.

The maximum outer diameter of each spiral waveguide is designed to be smaller than the writing-field size, as shown in Fig. 5.6(d), thereby ensuring that the entire spiral can be patterned without crossing writing-field boundaries. Within each writing field, the electron beam traces the waveguide path along its geometric layout, following the propagation direction of the waveguide during exposure. This approach helps maintain pattern fidelity and minimizes local exposure nonuniformities within each writing field.

Chapter 6

Future outlook

This thesis analyzes the frequency noise sources in semiconductor lasers and optical parametric oscillators, along with the theoretical predictions of their intrinsic linewidths. It also demonstrates how passive external cavities and self-injection locking technologies effectively suppress frequency noise. For the semiconductor laser noise suppression, a DFB laser is self-injection locked to low-loss silicon nitride microring resonators to achieve an intrinsic linewidth of 9 Hz. Although this technology has been realized in recent years, it is the first time it has been demonstrated in our laboratory. Regarding the linewidth reduction for soliton microcombs, the intrinsic linewidth of the comb lines is reduced to below 1 Hz through the use of an external low-loss and long fiber loop. This method is novel and simple, and its performance is comparable to that of current narrow-linewidth soliton microcombs. Furthermore, we develop a chip-scale integrated system in which the optical components are designed and implemented on chip, and a meter-scale low-loss feedback waveguide is fabricated. This work represents the first demonstration of a narrow-linewidth on-chip external-cavity optical parametric oscillator.

Future research can be carried out from the following aspects.

Firstly, when the DFB laser is coupled to a low-loss silicon nitride chip and the self-injection locked regime is overlapped with the soliton generation regime by adjusting the laser's driving current, temperature, a microcomb with narrow linewidth can be directly pumped by the DFB laser. This configuration has good repeatability and is plug-and-play, which can avoid the tediousness of other soliton generation methods. If self-injection locking can be used to achieve narrow-linewidth, high-efficiency ($> 50\%$) soliton microcombs in silicon nitride, it will be attrac-

tive.

The second is heterogeneous integrated soliton microcombs. Although heterogeneous integration is relatively mature as mentioned in Chapter 1, most of the researches are on thin silicon nitride platforms, and heterogeneous integration on dispersion-engineered silicon nitride platforms needs to be further improved. Based on the previous questions, if a fully on-chip narrow-linewidth and high-efficiency soliton microcomb can be realized, it will provide great help for future soliton applications.

Finally, the intrinsic linewidth of an integrated narrow-linewidth optical parametric oscillator can be further suppressed by increasing the length of the feedback waveguide. However, as the waveguide length increases, the accumulated propagation loss in the feedback waveguide will further reduce the feedback strength, which may limit the effectiveness of linewidth suppression. To compensate for this loss, an optical amplifier must be incorporated into the feedback loop. Although we have demonstrated that an erbium-doped Al_2O_3 waveguide amplifier can effectively enhance the feedback strength, the current implementation relies on fiber-based connections within the feedback circuit. To enable a fully integrated solution, a multilayer on-chip architecture can be employed. In this approach, the first layer consists of a Si_3N_4 platform that supports optical parametric oscillation and the feedback circuit. A second layer of erbium-doped Al_2O_3, deposited on top of the Si_3N_4, provides optical gain for the feedback signal. Furthermore, by heterogeneously integrating a semiconductor pump laser onto the same chip via micro-transfer printing, a fully integrated narrow-linewidth optical parametric oscillator can be realized.

Chapter 7

Summary of papers

Paper A

Low-loss dispersion-engineered silicon nitride waveguides coated with a thin blanket layer,
Conference on Lasers and Electro-Optics, San Jose, USA, paper JW3B.183, 2022.

In this work, we coated an 8 nm thick Si_3N_4 blanket layer on etched Si_3N_4 waveguides, and we found that the thin layer can effectively reduce the propagation loss in the highly confined Si_3N_4 waveguide, but does not affect the group velocity dispersion much.

My contributions: I performed simulations of the optical modes and dispersion of silicon nitride waveguides with various geometries, characterized the fabricated devices, and analyzed the measured data. In addition, I designed and fabricated new devices to further investigate and demonstrate the observed improvements. I wrote the paper with support from the co-authors and presented the work at CLEO 2022.

Paper B

High-power on-chip hyperparametric oscillator,
Optics Letters, vol. 50, no. 15, pp. 4798-4801, 2025.

In this work, we numerically demonstrated strong coupling and high pump power can provide high output power for optical hyperparametric oscillators. Microrings based on bound states in the continuum peri-

odically exhibit high intrinsic Q factors to suppress mode competition, thereby achieving high-efficiency. After optimization, we experimentally presented a high-power optical hyperparametric oscillator whose signal wave has an on-chip power of 215 mW and an intrinsic linewidth of 220 Hz.

My contributions: I carried out simulations of output power for various microring designs, followed by the fabrication and characterization of the corresponding devices. I investigated the sidewall roughness in ultra-narrow gaps between microring resonators and bus waveguides. I performed experiments to realize the desired performance. I wrote the manuscript with support from the co-authors.

Paper C

Self-injection-locked optical parametric oscillator based on microcombs,
Optica, vol. 11, no. 3, pp. 420-426, 2024.

In this work, we demonstrated a sub-Hz linewidth optical parametric oscillator through self-injection locking a single comb line from a soliton microcomb. We revealed a dynamic similar to that found in conventional lasers using self-injection locking and showed that there exists a dynamic regime where the frequency noise of the comb line can be consistently reduced to three orders of magnitude below the pump.

My contributions: I assisted in all experiments and independently conducted one of the experiments, analyzed the corresponding data, and prepared a figure for the manuscript. I also assisted in running simulations and writing the paper.

Paper D

Chip-scale narrow-linewidth optical parametric oscillators,
submitted, 2026.

In this work, we propose a novel design for an on-chip narrow-linewidth optical parametric oscillator. By introducing a meter-scale integrated external cavity that feeds the signal light back into the main

Kerr cavity, the frequency noise of the signal can be effectively reduced. Numerical simulations show that the frequency noise of the signal light can reach the hertz level or below. Experimentally, we achieved an intrinsic linewidth of 10 Hz using 1.5 m integrated waveguide feedback line. Furthermore, the intrinsic linewidth can be reduced to 0.6 Hz using a longer amplified loop.

My contributions: I proposed the design of the integrated narrow-linewidth optical parametric oscillator, performed numerical simulations of its frequency noise, and fabricated and characterized the corresponding devices. I also conducted experiments and developed measurement methods. I wrote the manuscript with support from the co-authors.

References

[1] A. Einstein, "Zur quantentheorie der strahlung," *Physikalische Zeitschrift*, vol. 18, p. 121, 1917.

[2] J. P. Gordon, H. J. Zeiger, and C. H. Townes, "The maser—new type of microwave amplifier, frequency standard, and spectrometer," *Physical Review*, vol. 99, no. 4, p. 1264, 1955.

[3] A. L. Schawlow and C. H. Townes, "Infrared and optical masers," *Physical Review*, vol. 112, no. 6, p. 1940, 1958.

[4] T. H. Maiman, "Stimulated optical radiation in ruby," *Nature*, vol. 187, no. 4736, pp. 493–494, 1960.

[5] A. Javan, W. R. Bennett Jr, and D. R. Herriott, "Population inversion and continuous optical maser oscillation in a gas discharge containing a He-Ne mixture," *Physical Review Letters*, vol. 6, no. 3, p. 106, 1961.

[6] R. N. Hall, G. E. Fenner, J. Kingsley, T. Soltys, and R. Carlson, "Coherent light emission from GaAs junctions," *Physical Review Letters*, vol. 9, no. 9, p. 366, 1962.

[7] G. P. Agrawal, *Fiber-optic communication systems.* John Wiley & Sons, 2012.

[8] M. Q. Chau, "An overview study on the laser technology and applications in the mechanical and machine manufacturing industry," *Journal of Mechanical Engineering Research and Developments*, vol. 42, no. 5, pp. 16–20, 2019.

[9] H. J. Metcalf and P. Van der Straten, *Laser cooling and trapping.* Springer Science & Business Media, 1999.

[10] K. F. Renk, *Basics of laser physics.* Springer, 2012.

[11] R. W. Boyd, A. L. Gaeta, and E. Giese, "Nonlinear optics," in *Springer Handbook of Atomic, Molecular, and Optical Physics.* Springer, 2008, pp. 1097–1110.

[12] I. Breunig, D. Haertle, and K. Buse, "Continuous-wave optical parametric oscillators: recent developments and prospects," *Applied Physics B*, vol. 105, pp. 99–111, 2011.

[13] X. Lu, R. M. Gray, J. Stone, S. Zhou, N. Englebert, A. Marandi, and K. Srinivasan, "Photonic integrated circuit optical parametric oscillators," *Optica*, vol. 13, no. 1, pp. 11–30, 2025.

[14] e. P. Franken, A. E. Hill, C. Peters, and G. Weinreich, "Generation of optical harmonics," *Physical Review Letters*, vol. 7, no. 4, p. 118, 1961.

[15] M. Vainio and L. Halonen, "Mid-infrared optical parametric oscillators and frequency combs for molecular spectroscopy," *Physical Chemistry Chemical Physics*, vol. 18, no. 6, pp. 4266–4294, 2016.

[16] R. V. Roussev, C. Langrock, J. R. Kurz, and M. M. Fejer, "Periodically poled lithium niobate waveguide sum-frequency generator for efficient single-photon detection at communication wavelengths," *Optics Letters*, vol. 29, no. 13, pp. 1518–1520, 2004.

[17] X. Luo, Z. Li, Y. Guo, J. Yao, and Y. Wu, "Recent progress on new infrared nonlinear optical materials with application prospect," *Journal of Solid State Chemistry*, vol. 270, pp. 674–687, 2019.

[18] R. R. Anderson and J. A. Parrish, "Selective photothermolysis: precise microsurgery by selective absorption of pulsed radiation," *Science*, vol. 220, no. 4596, pp. 524–527, 1983.

[19] Q. Cheng, M. Bahadori, M. Glick, S. Rumley, and K. Bergman, "Recent advances in optical technologies for data centers: a review," *Optica*, vol. 5, no. 11, pp. 1354–1370, 2018.

[20] K. Gasmi, A. Aljalal, and W. Al-Basheer, "Blue external-cavity diode laser for NO2 gas detection," in *Semiconductor Lasers and Laser Dynamics IX*, vol. 11356. SPIE, 2020, pp. 140–147.

[21] Q.-F. Yang, B. Shen, H. Wang, M. Tran, Z. Zhang, K. Y. Yang, L. Wu, C. Bao, J. Bowers, A. Yariv *et al.*, "Vernier spectrometer using counterpropagating soliton microcombs," *Science*, vol. 363, no. 6430, pp. 965–968, 2019.

[22] Y. Dai, T. Fu, J. Chen, C. Tang, X. Wang, Y. Wang, and W. Zheng, "High-power semiconductor laser with a narrow linewidth based on transverse photonic crystal," *Optics Express*, vol. 32, no. 20, pp. 36 010–36 020, 2024.

[23] H. Stoehr, F. Mensing, J. Helmcke, and U. Sterr, "Diode laser with 1 Hz linewidth," *Optics Letters*, vol. 31, no. 6, pp. 736–738, 2006.

[24] C. V. Poulton, M. J. Byrd, P. Russo, E. Timurdogan, M. Khandaker, D. Vermeulen, and M. R. Watts, "Long-range LiDAR and free-space data communication with high-performance optical phased arrays," *IEEE Journal of Selected Topics in Quantum Electronics*, vol. 25, no. 5, pp. 1–8, 2019.

[25] L. Krinner, K. Dietze, L. Pelzer, N. Spethmann, and P. Schmidt, "Low phase noise cavity transmission self-injection locked diode laser system for atomic physics experiments," *Optics Express*, vol. 32, no. 9, pp. 15 912–15 922, 2024.

[26] Q. Zhao, Z. Zhang, B. Wu, T. Tan, C. Yang, J. Gan, H. Cheng, Z. Feng, M. Peng, Z. Yang *et al.*, "Noise-sidebands-free and ultra-low-RIN 1.5 μm single-frequency fiber laser towards coherent optical detection," *Photonics Research*, vol. 6, no. 4, pp. 326–331, 2018.

[27] Z. L. Newman, V. Maurice, T. Drake, J. R. Stone, T. C. Briles, D. T. Spencer, C. Fredrick, Q. Li, D. Westly, B. R. Ilic *et al.*, "Architecture for the photonic integration of an optical atomic clock," *Optica*, vol. 6, no. 5, pp. 680–685, 2019.

[28] Z. Bai, Z. Zhao, M. Tian, D. Jin, Y. Pang, S. Li, X. Yan, Y. Wang, and Z. Lu, "A comprehensive review on the development and applications of narrow-linewidth lasers," *Microwave and Optical Technology Letters*, vol. 64, no. 12, pp. 2244–2255, 2022.

[29] Y. Peng, X. Wei, G. Xie, J. Gao, D. Li, and W. Wang, "A high-power narrow-linewidth optical parametric oscillator based on PP-MgLN," *Laser Physics*, vol. 23, no. 5, p. 055405, 2013.

[30] W. Wang, L. Wang, and W. Zhang, "Advances in soliton microcomb generation," *Advanced Photonics*, vol. 2, no. 3, pp. 034 001–034 001, 2020.

[31] Z. Zhou, X. Ou, Y. Fang, E. Alkhazraji, R. Xu, Y. Wan, and J. E. Bowers, "Prospects and applications of on-chip lasers," *Elight*, vol. 3, no. 1, p. 1, 2023.

[32] W. Liang, V. Ilchenko, D. Eliyahu, A. Savchenkov, A. Matsko, D. Seidel, and L. Maleki, "Ultralow noise miniature external cavity semiconductor laser," *Nature Communications*, vol. 6, no. 1, p. 7371, 2015.

[33] T. L. Koch and U. Koren, "Semiconductor lasers for coherent optical fiber communications," *Journal of Lightwave Technology*, vol. 8, no. 3, pp. 274–293, 1990.

[34] S. Selmic, S. L. Wilson, G. Evans, J. B. Kirk, Z. A. Alhilali, and D. Phan, "High-power single-frequency semiconductor lasers," in *2001 IEEE Emerging Technologies Symposium on BroadBand Communications for the Internet Era. Symposium Digest (Cat. No. 01EX508)*. IEEE, 2001, pp. 48–52.

[35] C. Henry, "Theory of the linewidth of semiconductor lasers," *IEEE Journal of Quantum Electronics*, vol. 18, no. 2, pp. 259–264, 1982.

[36] S. Wang, "Principles of distributed feedback and distributed Bragg-reflector lasers," *IEEE Journal of Quantum Electronics*, vol. 10, no. 4, pp. 413–427, 1974.

[37] H. Kogelnik and C. Shank, "Stimulated emission in a periodic structure," *Applied Physics Letters*, vol. 18, no. 4, pp. 152–154, 1971.

[38] Y. Yamamoto, S. Saito, and T. Mukai, "AM and FM quantum noise in semiconductor lasers-part II: comparison of theoretical and experimental results for AlGaAs lasers," *IEEE Journal of Quantum Electronics*, vol. 19, no. 1, pp. 47–58, 1983.

[39] T. Aoki, Y. Itoh, M. Ogasawara, K. Fujii, S. Kimura, Y. Sawada, H. Yoshinaga, N. Fujiwara, H. Yagi, M. Yanagisawa *et al.*, "Narrow-linewidth 1.55-μm-wavelength InP-based photonic-crystal surface-emitting lasers with near-diffraction-limited beam quality," *Optics Express*, vol. 33, no. 20, pp. 42 480–42 488, 2025.

[40] W. Streifer, R. Burnham, and D. Scifres, "Effect of external reflectors on longitudinal modes of distributed feedback lasers," *IEEE Journal of Quantum Electronics*, vol. 11, no. 4, pp. 154–161, 1975.

[41] S. Saito, O. Nilsson, and Y. Yamamoto, "Oscillation center frequency tuning, quantum FM noise, and direct frequency characteristics in external grating loaded semiconductor lasers," *IEEE Journal of Quantum Electronics*, vol. 18, no. 6, pp. 961–970, 1982.

[42] K. Choi, J. Menders, P. Searcy, and E. Korevaar, "Optical feedback locking of a diode laser using a cesium faraday filter," *Optics Communications*, vol. 96, no. 4-6, pp. 240–244, 1993.

[43] X. Zhang, N. Wang, L. Gao, M. Feng, B. Chen, Y. H. Tsang, and A. Liu, "Narrow-linewidth external-cavity tunable lasers," in *10th International Conference on Optical Communications and Networks (ICOCN 2011)*. IET, 2011, pp. 1–2.

[44] D. J. Thompson and R. E. Scholten, "Narrow linewidth tunable external cavity diode laser using wide bandwidth filter," *Review of Scientific Instruments*, vol. 83, no. 2, 2012.

[45] E. Patzak, H. Olesen, A. Sugimura, S. Saito, and T. Mukai, "Spectral linewidth reduction in semiconductor lasers by an external cavity with weak optical feedback," *Electronics Letters*, vol. 22, no. 19, pp. 938–940, 1983.

[46] H. Li and N. Abraham, "Analysis of the noise spectra of a laser diode with optical feedback from a high-finesse resonator," *IEEE Journal of Quantum Electronics*, vol. 25, no. 8, pp. 1782–1793, 1989.

[47] J. Lawrence and D. Kane, "Injection locking suppression of coherence collapse in a diode laser with optical feedback," *Optics communications*, vol. 167, no. 1-6, pp. 273–282, 1999.

[48] F. Wang, G. Zhao, J. Meng, G. Liu, and Z. Liu, "Widely tunable narrow-linewidth ZGP optical parametric oscillator with injection of single frequency seed," *Optics & Laser Technology*, vol. 181, p. 111834, 2025.

[49] Y. Song, Z. Yu, S. Li, M. Wang, X. Zhu, J. Liu, X. Hou, and W. Chen, "Tunable and injection-seeded operation of a narrow-linewidth BBO optical parametric oscillator pumped by 355 nm laser," *Optics & Laser Technology*, vol. 192, p. 113671, 2025.

[50] R. Li, S. Huang, H. Nie, J. Zhang, T. Ma, J. Zhang, Z. Chen, C. Jia, B. Yao, J. Xia *et al.*, "High power narrow bandwidth picosecond PPLN-OPO," *Optics Express*, vol. 33, no. 11, pp. 24 178–24 184, 2025.

[51] M. Henriksson, L. Sjöqvist, V. Pasiskevicius, and F. Laurell, "Narrow linewidth 2 μm optical parametric oscillation in periodically poled LiNbO3 with volume Bragg grating outcoupler," *Applied Physics B*, vol. 86, no. 3, pp. 497–501, 2007.

[52] F. Ganikhanov, T. Caughey, and K. Vodopyanov, "Narrow-linewidth middle-infrared ZnGeP2 optical parametric oscillator," *Journal of the Optical Society of America B*, vol. 18, no. 6, pp. 818–822, 2001.

[53] B. Jacobsson, M. Tiihonen, V. Pasiskevicius, and F. Laurell, "Narrowband bulk Bragg grating optical parametric oscillator," *Optics Letters*, vol. 30, no. 17, pp. 2281–2283, 2005.

[54] M. Vainio, C. Ozanam, V. Ulvila, and L. Halonen, "Tuning and stability of a singly resonant continuous-wave optical parametric oscillator close to degeneracy," *Optics Express*, vol. 19, no. 23, pp. 22 515–22 527, 2011.

[55] J. Saikawa, M. Fujii, H. Ishizuki, and T. Taira, "High-energy, narrow-bandwidth periodically poled Mg-doped LiNbO3 optical parametric oscillator with a volume bragg grating," *Optics Letters*, vol. 32, no. 20, pp. 2996–2998, 2007.

[56] I. Ricciardi, E. De Tommasi, P. Maddaloni, S. Mosca, A. Rocco, J.-J. Zondy, M. De Rosa, and P. De Natale, "A narrow-linewidth optical parametric oscillator for mid-infrared high-resolution spectroscopy," *Molecular Physics*, vol. 110, no. 17, pp. 2103–2109, 2012.

[57] W. Wang, X. Jin, M. Sun, R. Zhao, Z. Wang, H. Liu, and Y. Yu, "Study on narrow linewidth 2.1 μm self-optical parametric oscillator based on Nd: MgO: PPLN," *Infrared Physics & Technology*, vol. 140, p. 105415, 2024.

[58] G. Zhong, B. Lu, H. Liu, Y. Yu, and G. Jin, "Mid-infrared narrow-linewidth wavelength tuning in MgO: PPLN optical parametric oscillation," *Infrared Physics & Technology*, p. 105943, 2025.

[59] J. Bian, H. Kong, Q. Ye, J. Yao, L. Guo, and X. Sun, "Narrow-linewidth BaGa4Se7 optical parametric oscillator," *Chinese Optics Letters*, vol. 20, no. 4, p. 041901, 2022.

[60] L. Zhang, S. Hong, Y. Wang, H. Yan, Y. Xie, T. Chen, M. Zhang, Z. Yu, Y. Shi, L. Liu *et al.*, "Ultralow-loss silicon photonics beyond the singlemode regime," *Laser & Photonics Reviews*, vol. 16, no. 4, p. 2100292, 2022.

[61] M. J. Heck, J. F. Bauters, M. L. Davenport, D. T. Spencer, and J. E. Bowers, "Ultra-low loss waveguide platform and its integration with silicon photonics," *Laser & Photonics Reviews*, vol. 8, no. 5, pp. 667–686, 2014.

[62] D. Zeng, Q. Liu, C. Mei, H. Li, Q. Huang, and X. Zhang, "Demonstration of ultra-High-Q silicon microring resonators for nonlinear integrated photonics," *Micromachines*, vol. 13, no. 7, p. 1155, 2022.

[63] M. W. Puckett, K. Liu, N. Chauhan, Q. Zhao, N. Jin, H. Cheng, J. Wu, R. O. Behunin, P. T. Rakich, K. D. Nelson *et al.*, "422 million intrinsic quality factor planar integrated all-waveguide resonator with sub-MHz linewidth," *Nature Communications*, vol. 12, no. 1, p. 934, 2021.

[64] X. Ji, F. A. Barbosa, S. P. Roberts, A. Dutt, J. Cardenas, Y. Okawachi, A. Bryant, A. L. Gaeta, and M. Lipson, "Ultra-low-loss on-chip resonators with sub-milliwatt parametric oscillation threshold," *Optica*, vol. 4, no. 6, pp. 619–624, 2017.

[65] D. T. Spencer, J. F. Bauters, M. J. Heck, and J. E. Bowers, "Integrated waveguide coupled Si3N4 resonators in the ultrahigh-Q regime," *Optica*, vol. 1, no. 3, pp. 153–157, 2014.

[66] Z. Ye, "Ultralow-loss silicon nitride waveguides for nonlinear optics," Ph.D. dissertation, Chalmers Tekniska Hogskola (Sweden), 2021.

[67] J. Liu, G. Huang, R. N. Wang, J. He, A. S. Raja, T. Liu, N. J. Engelsen, and T. J. Kippenberg, "High-yield, wafer-scale fabrication of ultralow-loss, dispersion-engineered silicon nitride photonic circuits," *Nature Communications*, vol. 12, no. 1, p. 2236, 2021.

[68] Z. Ye, K. Twayana, P. A. Andrekson, and V. Torres-Company, "High-Q Si3N4 microresonators based on a subtractive processing for Kerr nonlinear optics," *Optics Express*, vol. 27, no. 24, pp. 35 719–35 727, 2019.

[69] T. J. Kippenberg, S. M. Spillane, D. K. Armani, and K. J. Vahala, "Fabrication and coupling to planar high-Q silica disk microcavities," *Applied Physics Letters*, vol. 83, no. 4, pp. 797–799, 2003.

[70] T. J. Kippenberg, S. M. Spillane, and K. J. Vahala, "Kerr-nonlinearity optical parametric oscillation in an ultrahigh-Q toroid microcavity," *Physical Review Letters*, vol. 93, no. 8, p. 083904, 2004.

[71] R. J. Deri and E. Kapon, "Low-loss III-V semiconductor optical waveguides," *IEEE Journal of Quantum Electronics*, vol. 27, no. 3, pp. 626–640, 1991.

[72] C. Ciminelli, D. D'Agostino, G. Carnicella, F. Dell'Olio, D. Conteduca, H. P. Ambrosius, M. K. Smit, and M. N. Armenise, "A high-Q InP resonant angular velocity sensor for a monolithically integrated optical gyroscope," *IEEE Photonics Journal*, vol. 8, no. 1, pp. 1–19, 2015.

[73] M. Zhang, C. Wang, R. Cheng, A. Shams-Ansari, and M. Lončar, "Monolithic ultra-high-Q lithium niobate microring resonator," *Optica*, vol. 4, no. 12, pp. 1536–1537, 2017.

[74] Y. Gao, F. Lei, M. Girardi, Z. Ye, R. Van Laer, V. Torres-Company, and J. Schröder, "Compact lithium niobate microring resonators in the ultrahigh Q/V regime," *Optics Letters*, vol. 48, no. 15, pp. 3949–3952, 2023.

[75] Y. Fan, A. van Rees, P. J. Van der Slot, J. Mak, R. M. Oldenbeuving, M. Hoekman, D. Geskus, C. G. Roeloffzen, and K.-J. Boller, "Hybrid integrated InP-Si3N4 diode laser with a 40-Hz intrinsic linewidth," *Optics Express*, vol. 28, no. 15, pp. 21 713–21 728, 2020.

[76] Y. Fan, R. M. Oldenbeuving, E. J. Klein, C. J. Lee, H. Song, M. R. Khan, H. L. Offerhaus, P. J. van der Slot, and K.-J. Boller, "A hybrid semiconductor-glass waveguide laser," in *Laser Sources and Applications II*, vol. 9135. SPIE, 2014, pp. 231–236.

[77] B. Li, W. Jin, L. Wu, L. Chang, H. Wang, B. Shen, Z. Yuan, A. Feshali, M. Paniccia, K. J. Vahala *et al.*, "Reaching fiber-laser coherence in integrated photonics," *Optics Letters*, vol. 46, no. 20, pp. 5201–5204, 2021.

[78] C. A. Franken, W. A. Hendriks, L. V. Winkler, A. do Nascimento Jr, A. van Rees, M. Dijkstra, S. Mardani, D. Kienzler, R. Dekker, J. van Kerkhof *et al.*, "Widely tunable and narrow-linewidth violet lasers enabled by UV-transparent materials," *Nature Communications*, vol. 16, no. 1, p. 10294, 2025.

[79] M. A. Tran, D. Huang, J. Guo, T. Komljenovic, P. A. Morton, and J. E. Bowers, "Ring-resonator based widely-tunable narrow-linewidth Si/InP integrated lasers," *IEEE Journal of Selected Topics in Quantum Electronics*, vol. 26, no. 2, pp. 1–14, 2019.

[80] C. Xiang, W. Jin, O. Terra, B. Dong, H. Wang, L. Wu, J. Guo, T. J. Morin, E. Hughes, J. Peters *et al.*, "3D integration enables ultralow-noise isolator-free lasers in silicon photonics," *Nature*, vol. 620, no. 7972, pp. 78–85, 2023.

[81] C. Xiang, W. Jin, J. Guo, J. D. Peters, M. Kennedy, J. Selvidge, P. A. Morton, and J. E. Bowers, "Narrow-linewidth III-V/Si/Si3N4 laser using multilayer heterogeneous integration," *Optica*, vol. 7, no. 1, pp. 20–21, 2020.

[82] K.-J. Boller, A. van Rees, Y. Fan, J. Mak, R. E. Lammerink, C. A. Franken, P. J. van der Slot, D. A. Marpaung, C. Fallnich, J. P. Epping *et al.*, "Hybrid integrated semiconductor lasers with silicon nitride feedback circuits," in *Photonics*, vol. 7, no. 1. Multidisciplinary Digital Publishing Institute, 2020, p. 4.

[83] W. Jin, Q.-F. Yang, L. Chang, B. Shen, H. Wang, M. A. Leal, L. Wu, M. Gao, A. Feshali, M. Paniccia *et al.*, "Hertz-linewidth semiconductor lasers using CMOS-ready ultra-high-Q microresonators," *Nature Photonics*, vol. 15, no. 5, pp. 346–353, 2021.

[84] C. Xiang, J. Liu, J. Guo, L. Chang, R. N. Wang, W. Weng, J. Peters, W. Xie, Z. Zhang, J. Riemensberger *et al.*, "Laser soliton microcombs heterogeneously integrated on silicon," *Science*, vol. 373, no. 6550, pp. 99–103, 2021.

[85] C. Xiang, W. Jin, and J. E. Bowers, "Silicon nitride passive and active photonic integrated circuits: trends and prospects," *Photonics Research*, vol. 10, no. 6, pp. A82–A96, 2022.

[86] E. Alkhazraji, W. W. Chow, F. Grillot, J. E. Bowers, and Y. Wan, "Linewidth narrowing in self-injection-locked on-chip lasers," *Light: Science & Applications*, vol. 12, no. 1, p. 162, 2023.

[87] C. Zhang, M. A. Tran, Z. Zhang, A. E. Dorche, Y. Shen, B. Shen, K. Asawa, G. Kim, N. Kim, F. Levinson *et al.*, "Integrated photonics beyond communications," *Applied Physics Letters*, vol. 123, no. 23, 2023.

[88] A. Malik, C. Xiang, L. Chang, W. Jin, J. Guo, M. Tran, and J. Bowers, "Low noise, tunable silicon photonic lasers," *Applied Physics Reviews*, vol. 8, no. 3, 2021.

[89] N. Singh, J. Lorenzen, K. Wang, M. A. Gaafar, M. Sinobad, H. Francis, M. Edelmann, M. Geiselmann, T. Herr, S. M. Garcia-Blanco *et al.*, "Watt-class silicon photonics-based optical high-power amplifier," *Nature Photonics*, vol. 19, no. 3, pp. 307–314, 2025.

[90] N. Singh, J. Lorenzen, M. Sinobad, K. Wang, A. C. Liapis, H. C. Frankis, S. Haugg, H. Francis, J. Carreira, M. Geiselmann *et al.*, "Silicon photonics-based high-energy passively Q-switched laser," *Nature Photonics*, vol. 18, no. 5, pp. 485–491, 2024.

[91] Y. Sun, J. Sulhoff, A. Srivastava, J. Zyskind, T. Strasser, J. Pedrazzani, C. Wolf, J. Zhou, J. Judkins, R. Espindola *et al.*, "80 nm ultra-wideband erbium-doped silica fibre amplifier," *Electronics Letters*, vol. 33, no. 23, pp. 1965–1967, 1997.

[92] A. Polman, "Erbium implanted thin film photonic materials," *Journal of Applied Physics*, vol. 82, no. 1, pp. 1–39, 1997.

[93] A. Kenyon, "Recent developments in rare-earth doped materials for optoelectronics," *Progress in Quantum Electronics*, vol. 26, no. 4-5, pp. 225–284, 2002.

[94] Y. Liu, Z. Qiu, X. Ji, A. Lukashchuk, J. He, J. Riemensberger, M. Hafermann, R. N. Wang, J. Liu, C. Ronning *et al.*, "A photonic integrated circuit–based erbium-doped amplifier," *Science*, vol. 376, no. 6599, pp. 1309–1313, 2022.

[95] Y. Liu, Z. Qiu, X. Ji, A. Bancora, G. Lihachev, J. Riemensberger, R. N. Wang, A. Voloshin, and T. J. Kippenberg, "A fully hybrid integrated erbium-based laser," *Nature Photonics*, vol. 18, no. 8, pp. 829–835, 2024.

[96] J. Zhou, Y. Liang, Z. Liu, W. Chu, H. Zhang, D. Yin, Z. Fang, R. Wu, J. Zhang, W. Chen *et al.*, "On-chip integrated waveguide amplifiers on erbium-doped thin-film lithium niobate on insulator," *Laser & Photonics Reviews*, vol. 15, no. 8, p. 2100030, 2021.

[97] Y. Ma, M. Li, J. Yu, Z. Fang, M. Wang, J. Lin, H. Zhang, and Y. Cheng, "High external power narrow bandwidth erbium doped waveguide laser on thin film lithium niobate," *Nanophotonics*, vol. 14, no. 26, pp. 4703–4711, 2025.

[98] C. Osornio-Martinez, D. Bonneville, M. Dijkstra, A. do Nascimento Jr, and S. Garcia-Blanco, "Broadband packaged erbium-eoped polycrystalline Al2O3 waveguide amplifier with 24 dB external net gain," *Optics Express*, vol. 33, no. 14, pp. 28 985–28 994, 2025.

[99] J. Liu, Q. Hou, Y. Zhou, Q. Dai, Z. Liu, M. Wang, R. Gao, Z. Fang, J. Lin, and Y. Cheng, "On-chip microlaser and waveguide amplifier on thin-film erbium-doped tantalum pentoxide," *Chinese Optics Letters*, vol. 23, no. 7, p. 071302, 2025.

[100] J. D. Bradley and M. Pollnau, "Erbium-doped integrated waveguide amplifiers and lasers," *Laser & Photonics Reviews*, vol. 5, no. 3, pp. 368–403, 2011.

[101] X. Ji, X. Yang, Y. Liu, Z. Qiu, G. Lihachev, S. Bianconi, J. Sun, A. Voloshin, T. Kim, J. C. Olson *et al.*, "Full C-and L-band tunable erbium-doped integrated lasers via scalable manufacturing," *arXiv preprint arXiv:2501.06936*, 2025.

[102] F. Lei, Z. Ye, K. Twayana, Y. Gao, M. Girardi, Ó. B. Helgason, P. Zhao, and V. Torres-Company, "Hyperparametric oscillation via

bound states in the continuum," *Physical Review Letters*, vol. 130, no. 9, p. 093801, 2023.

[103] F. Riehle, *Frequency standards: basics and applications.* John Wiley & Sons, 2006.

[104] Z. Fang, H. Cai, G. Chen, and R. Qu, *Single frequency semiconductor lasers.* Springer, 2017.

[105] M. A. Tran, D. Huang, and J. E. Bowers, "Tutorial on narrow linewidth tunable semiconductor lasers using Si/III-V heterogeneous integration," *APL Photonics*, vol. 4, no. 11, 2019.

[106] G. Di Domenico, S. Schilt, and P. Thomann, "Simple approach to the relation between laser frequency noise and laser line shape," *Applied Optics*, vol. 49, no. 25, pp. 4801–4807, 2010.

[107] D. Elliott, R. Roy, and S. Smith, "Extracavity laser band-shape and bandwidth modification," *Physical Review A*, vol. 26, no. 1, p. 12, 1982.

[108] G. M. Stéphan, T. Tam, S. Blin, P. Besnard, and M. Têtu, "Laser line shape and spectral density of frequency noise," *Physical Review A—Atomic, Molecular, and Optical Physics*, vol. 71, no. 4, p. 043809, 2005.

[109] K. Kikuchi, "Impact of 1/f-type FM noise on coherent optical communications," *Electronics Letters*, vol. 17, no. 23, pp. 885–887, 1987.

[110] J. Ohtsubo and J. Ohtsubo, *Semiconductor lasers and theory.* Springer, 2017.

[111] L. A. Coldren, S. W. Corzine, and M. L. Mashanovitch, *Diode lasers and photonic integrated circuits.* John Wiley & Sons, 2012, vol. 218.

[112] K. Vahala and A. Yariv, "Semiclassical theory of noise in semiconductor lasers-part I," *IEEE Journal of Quantum Electronics*, vol. 19, no. 6, pp. 1096–1101, 1983.

[113] C. Henry, "Theory of the phase noise and power spectrum of a single mode injection laser," *IEEE Journal of Quantum Electronics*, vol. 19, no. 9, pp. 1391–1397, 1983.

[114] C. Henry, "Phase noise in semiconductor lasers," *Journal of Lightwave Technology*, vol. 4, no. 3, pp. 298–311, 1986.

[115] K. Petermann, *Laser diode modulation and noise.* Springer Science & Business Media, 1991, vol. 3.

[116] H. Shu, L. Chang, Y. Tao, B. Shen, W. Xie, M. Jin, A. Netherton, Z. Tao, X. Zhang, R. Chen *et al.*, "Microcomb-driven silicon photonic systems," *Nature*, vol. 605, no. 7910, pp. 457–463, 2022.

[117] G. Moille, J. Stone, M. Chojnacky, R. Shrestha, U. A. Javid, C. Menyuk, and K. Srinivasan, "Kerr-induced synchronization of a cavity soliton to an optical reference," *Nature*, vol. 624, no. 7991, pp. 267–274, 2023.

[118] T. Herr, V. Brasch, J. D. Jost, C. Y. Wang, N. M. Kondratiev, M. L. Gorodetsky, and T. J. Kippenberg, "Temporal solitons in optical microresonators," *Nature Photonics*, vol. 8, no. 2, pp. 145–152, 2014.

[119] T. Herr, M. L. Gorodetsky, and T. J. Kippenberg, "Dissipative Kerr solitons in optical microresonators," *Nonlinear Optical Cavity Dynamics: from Microresonators to Fiber Lasers*, pp. 129–162, 2016.

[120] O. Svelto, D. C. Hanna *et al.*, *Principles of lasers.* Springer, 2010, vol. 1.

[121] P. Liao, C. Bao, A. Kordts, M. Karpov, M. H. Pfeiffer, L. Zhang, A. Mohajerin-Ariaei, Y. Cao, A. Almaiman, M. Ziyadi *et al.*, "Dependence of a microresonator Kerr frequency comb on the pump linewidth," *Optics Letters*, vol. 42, no. 4, pp. 779–782, 2017.

[122] M. Karpov, H. Guo, A. Kordts, V. Brasch, M. H. Pfeiffer, M. Zervas, M. Geiselmann, and T. J. Kippenberg, "Raman self-frequency shift of dissipative Kerr solitons in an optical microresonator," *Physical Review Letters*, vol. 116, no. 10, p. 103902, 2016.

[123] Q.-F. Yang, X. Yi, K. Y. Yang, and K. Vahala, "Spatial-mode-interaction-induced dispersive waves and their active tuning in microresonators," *Optica*, vol. 3, no. 10, pp. 1132–1135, 2016.

[124] F. Lei, Z. Ye, Ó. B. Helgason, A. Fülöp, M. Girardi, and V. Torres-Company, "Optical linewidth of soliton microcombs," *Nature Communications*, vol. 13, no. 1, p. 3161, 2022.

[125] A. B. Matsko and L. Maleki, "On timing jitter of mode locked Kerr frequency combs," *Optics Express*, vol. 21, no. 23, pp. 28 862–28 876, 2013.

[126] C. Bao, M.-G. Suh, B. Shen, K. Şafak, A. Dai, H. Wang, L. Wu, Z. Yuan, Q.-F. Yang, A. B. Matsko *et al.*, "Quantum diffusion of microcavity solitons," *Nature Physics*, vol. 17, no. 4, pp. 462–466, 2021.

[127] A. Chijioke, Q.-F. Chen, A. Y. Nevsky, and S. Schiller, "Thermal noise of whispering-gallery resonators," *Physical Review A—Atomic, Molecular, and Optical Physics*, vol. 85, no. 5, p. 053814, 2012.

[128] N. Kondratiev and M. Gorodetsky, "Thermorefractive noise in whispering gallery mode microresonators: analytical results and numerical simulation," *Physics Letters A*, vol. 382, no. 33, pp. 2265–2268, 2018.

[129] C. Panuski, D. Englund, and R. Hamerly, "Fundamental thermal noise limits for optical microcavities," *Physical Review X*, vol. 10, no. 4, p. 041046, 2020.

[130] M. L. Gorodetsky and I. S. Grudinin, "Fundamental thermal fluctuations in microspheres," *Journal of the Optical Society of America B*, vol. 21, no. 4, pp. 697–705, 2004.

[131] G. Huang, E. Lucas, J. Liu, A. S. Raja, G. Lihachev, M. L. Gorodetsky, N. J. Engelsen, and T. J. Kippenberg, "Thermorefractive noise in silicon-nitride microresonators," *Physical Review A*, vol. 99, no. 6, p. 061801, 2019.

[132] S. Dwivedi, A. Ruocco, M. Vanslembrouck, T. Spuesens, P. Bienstman, P. Dumon, T. Van Vaerenbergh, and W. Bogaerts, "Experimental extraction of effective refractive index and thermo-optic coefficients of silicon-on-insulator waveguides using interferometers," *Journal of Lightwave Technology*, vol. 33, no. 21, pp. 4471–4477, 2015.

[133] J.-Q. Chen, C. Chen, J.-J. Sun, J.-W. Zhang, Z.-H. Liu, L. Qin, Y.-Q. Ning, and L.-J. Wang, "Linewidth measurement of a narrow-linewidth laser: principles, methods, and systems," *Sensors*, vol. 24, no. 11, p. 3656, 2024.

[134] Z. Yuan, H. Wang, P. Liu, B. Li, B. Shen, M. Gao, L. Chang, W. Jin, A. Feshali, M. Paniccia *et al.*, "Correlated self-heterodyne method for ultra-low-noise laser linewidth measurements," *Optics Express*, vol. 30, no. 14, pp. 25 147–25 161, 2022.

[135] J. W. Dawson, N. Park, and K. J. Vahala, "An improved delayed self-heterodyne interferometer for linewidth measurements," *IEEE Photonics Technology Letters*, vol. 4, no. 9, pp. 1063–1066, 1992.

[136] Z. Zhao, Z. Bai, D. Jin, Y. Qi, J. Ding, B. Yan, Y. Wang, Z. Lu, and R. P. Mildren, "Narrow laser-linewidth measurement using short delay self-heterodyne interferometry," *Optics Express*, vol. 30, no. 17, pp. 30 600–30 610, 2022.

[137] E. Patzak, A. Sugimura, S. Saito, T. Mukai, and H. Olesen, "Semiconductor laser linewidth in optical feedback configurations," *Electronics Letters*, vol. 19, no. 24, pp. 1026–1027, 1983.

[138] R. Kazarinov and C. Henry, "The relation of line narrowing and chirp reduction resulting from the coupling of a semiconductor laser to passive resonator," *IEEE Journal of Quantum Electronics*, vol. 23, no. 9, pp. 1401–1409, 1987.

[139] T. Komljenovic and J. E. Bowers, "Monolithically integrated high-Q rings for narrow linewidth widely tunable lasers," *IEEE Journal of Quantum Electronics*, vol. 51, no. 11, pp. 1–10, 2015.

[140] K. Petermann, "External optical feedback phenomena in semiconductor lasers," *IEEE Journal of Selected Topics in Quantum Electronics*, vol. 1, no. 2, pp. 480–489, 1995.

[141] N. Schunk and K. Petermann, "Numerical analysis of the feedback regimes for a single-mode semiconductor laser with external feedback," *IEEE Journal of Quantum Electronics*, vol. 24, no. 7, pp. 1242–1247, 1988.

[142] K. Kikuchi and T. Okoshi, "Simple formula giving spectrum-narrowing ratio of semiconductor-laser output obtained by optical feedback," *Electronics Letters*, vol. 18, no. 1, pp. 10–12, 1982.

[143] P. Laurent, A. Clairon, and C. Breant, "Frequency noise analysis of optically self-locked diode lasers," *IEEE Journal of Quantum Electronics*, vol. 25, no. 6, pp. 1131–1142, 1989.

[144] N. Kondratiev, V. Lobanov, A. Cherenkov, A. Voloshin, N. Pavlov, S. Koptyaev, and M. Gorodetsky, "Self-injection locking of a laser diode to a high-Q WGM microresonator," *Optics Express*, vol. 25, no. 23, pp. 28 167–28 178, 2017.

[145] A. Li, T. Van Vaerenbergh, P. De Heyn, P. Bienstman, and W. Bogaerts, "Backscattering in silicon microring resonators: a quantitative analysis," *Laser & Photonics Reviews*, vol. 10, no. 3, pp. 420–431, 2016.

[146] R. R. Galiev, N. M. Kondratiev, V. E. Lobanov, A. B. Matsko, and I. A. Bilenko, "Optimization of laser stabilization via self-injection locking to a whispering-gallery-mode microresonator," *Physical Review Applied*, vol. 14, no. 1, p. 014036, 2020.

[147] A. E. Shitikov, I. I. Lykov, O. V. Benderov, D. A. Chermoshentsev, I. K. Gorelov, A. N. Danilin, R. R. Galiev, N. M. Kondratiev, S. J. Cordette, A. V. Rodin *et al.*, "Optimization of laser stabilization via self-injection locking to a whispering-gallery-mode microresonator: experimental study," *Optics Express*, vol. 31, no. 1, pp. 313–327, 2022.

[148] B. Stern, X. Ji, A. Dutt, and M. Lipson, "Compact narrow-linewidth integrated laser based on a low-loss silicon nitride ring resonator," *Optics Letters*, vol. 42, no. 21, pp. 4541–4544, 2017.

[149] B. Shen, X. Zhang, Y. Wang, Z. Tao, H. Shu, H. Chang, W. Li, Y. Zhou, Z. Ge, R. Chen *et al.*, "Reliable intracavity reflection for self-injection locking lasers and microcomb generation," *Photonics Research*, vol. 12, no. 5, pp. A41–A50, 2024.

[150] N. M. Kondratiev, V. E. Lobanov, A. E. Shitikov, R. R. Galiev, D. A. Chermoshentsev, N. Y. Dmitriev, A. N. Danilin, E. A. Lonshakov, K. N. Min'kov, D. M. Sokol *et al.*, "Recent advances in laser self-injection locking to high-Q microresonators," *Frontiers of Physics*, vol. 18, no. 2, p. 21305, 2023.

[151] D. A. Heim, D. Bose, K. Liu, A. Isichenko, and D. J. Blumenthal, "Hybrid integrated ultra-low linewidth coil stabilized isolator-free widely tunable external cavity laser," *Nature Communications*, vol. 16, no. 1, p. 5944, 2025.

[152] M. Haverlag, D. Vender, and G. Oehrlein, "Ellipsometric study of silicon surface damage in electron cyclotron resonance plasma etching using CF4 and SF6," *Applied Physics Letters*, vol. 61, no. 24, pp. 2875–2877, 1992.

[153] M. Borselli, T. J. Johnson, and O. Painter, "Beyond the rayleigh scattering limit in high-Q silicon microdisks: theory and experiment," *Optics Express*, vol. 13, no. 5, pp. 1515–1530, 2005.

[154] M. Gao, Q.-F. Yang, Q.-X. Ji, H. Wang, L. Wu, B. Shen, J. Liu, G. Huang, L. Chang, W. Xie *et al.*, "Probing material absorption and optical nonlinearity of integrated photonic materials," *Nature Communications*, vol. 13, no. 1, p. 3323, 2022.

[155] A. Gondarenko, J. S. Levy, and M. Lipson, "High confinement micron-scale silicon nitride high Q ring resonator," *Optics Express*, vol. 17, no. 14, pp. 11 366–11 370, 2009.

[156] M. H. Pfeiffer, J. Liu, A. S. Raja, T. Morais, B. Ghadiani, and T. J. Kippenberg, "Ultra-smooth silicon nitride waveguides based on the Damascene reflow process: fabrication and loss origins," *Optica*, vol. 5, no. 7, pp. 884–892, 2018.

[157] X. Ji, S. Roberts, M. Corato-Zanarella, and M. Lipson, "Methods to achieve ultra-high quality factor silicon nitride resonators," *APL Photonics*, vol. 6, no. 7, 2021.

[158] K. N. Andersen, W. E. Svendsen, T. Stimpel-Lindner, T. Sulima, and H. Baumgärtner, "Annealing and deposition effects of the chemical composition of silicon-rich nitride," *Applied Surface Science*, vol. 243, no. 1-4, pp. 401–408, 2005.

[159] Z. Ye, A. Fülöp, Ó. B. Helgason, P. A. Andrekson, and V. Torres-Company, "Low-loss high-Q silicon-rich silicon nitride microresonators for kerr nonlinear optics," *Optics Letters*, vol. 44, no. 13, pp. 3326–3329, 2019.

[160] X. Ji, J. K. Jang, U. D. Dave, M. Corato-Zanarella, C. Joshi, A. L. Gaeta, and M. Lipson, "Exploiting ultralow loss multimode waveguides for broadband frequency combs," *Laser & Photonics Reviews*, vol. 15, no. 1, p. 2000353, 2021.

[161] C. Yang and J. Pham, "Characteristic study of silicon nitride films deposited by LPCVD and PECVD," *Silicon*, vol. 10, no. 6, pp. 2561–2567, 2018.

[162] C. G. Roeloffzen, M. Hoekman, E. J. Klein, L. S. Wevers, R. B. Timens, D. Marchenko, D. Geskus, R. Dekker, A. Alippi, R. Grootjans *et al.*, "Low-loss Si3N4 TriPleX optical waveguides: technology and applications overview," *IEEE Journal of Selected Topics in Quantum Electronics*, vol. 24, no. 4, pp. 1–21, 2018.

[163] K. H. Nam, I. H. Park, and S. H. Ko, "Patterning by controlled cracking," *Nature*, vol. 485, no. 7397, pp. 221–224, 2012.

[164] K. Wu and A. W. Poon, "Stress-released Si3N4 fabrication process for dispersion-engineered integrated silicon photonics," *Optics Express*, vol. 28, no. 12, pp. 17 708–17 722, 2020.

[165] J. P. Epping, M. Hoekman, R. Mateman, A. Leinse, R. G. Heideman, A. van Rees, P. J. van der Slot, C. J. Lee, and K.-J. Boller, "High confinement, high yield Si3N4 waveguides for nonlinear optical applications," *Optics Express*, vol. 23, no. 2, pp. 642–648, 2015.

[166] C. J. Krückel, A. Fülöp, Z. Ye, P. A. Andrekson, and V. Torres-Company, "Optical bandgap engineering in nonlinear silicon nitride waveguides," *Optics Express*, vol. 25, no. 13, pp. 15 370–15 380, 2017.

[167] R. J. Bojko, J. Li, L. He, T. Baehr-Jones, M. Hochberg, and Y. Aida, "Electron beam lithography writing strategies for low loss, high confinement silicon optical waveguides," *Journal of Vacuum Science & Technology B*, vol. 29, no. 6, 2011.

[168] M. Girardi, *Wafer level processing of ultralow loss Si3N4*. Chalmers University of Technology, 2023.

[169] X. Zhang, Y. Liang, Y. Chen, B. Shen, J. Huang, C. Lao, Y. Wu, Z. Li, D. Liu, H. Shu *et al.*, "300-nm-thick, ultralow-loss silicon nitride photonic integrated circuits by 8-in. foundry production," *Applied Physics Letters*, vol. 125, no. 12, 2024.

[170] B. Kim, K.-H. Kwon, and S.-H. Park, "Characterizing metal-masked silica etch process in a CHF3/CF4 inductively coupled plasma," *Journal of Vacuum Science & Technology A: Vacuum, Surfaces, and Films*, vol. 17, no. 5, pp. 2593–2597, 1999.

[171] W.-T. Li, D. Bulla, and R. Boswell, "Surface oxidation of Al masks for deep dry-etch of silica optical waveguides," *Surface and Coatings Technology*, vol. 201, no. 9-11, pp. 4979–4983, 2007.

[172] A. L. Bogdanov, J. Lapointe, and J. H. Schmid, "Electron-beam lithography for photonic waveguide fabrication: Measurement of the effect of field stitching errors on optical performance and evaluation of a new compensation method," *Journal of Vacuum Science & Technology B*, vol. 30, no. 3, 2012.

[173] Z. Ye, F. Lei, K. Twayana, M. Girardi, P. A. Andrekson, and V. Torres-Company, "Integrated, ultra-compact high-Q silicon nitride microresonators for low-repetition-rate soliton microcombs," *Laser & Photonics Reviews*, vol. 16, no. 3, p. 2100147, 2022.

Papers

Paper A

Low-loss dispersion-engineered silicon nitride waveguides coated with a thin blanket layer

Yi Sun, Zhichao Ye, Raphaël Van Laer, Anders Larsson, and Victor Torres-Company

Conference on Lasers and Electro-Optics, San Jose, USA, paper JW3B.183, 2022.

Paper B

High-power on-chip hyperparametric oscillator

Yi Sun, Fuchuan Lei, Yan Gao, and Victor Torres-Company

Optics Letters, vol. 50, no. 15, pp. 4798-4801, 2025.

Paper C

Self-injection-locked optical parametric oscillator based on microcombs

Fuchuan Lei, **Yi Sun**, Óskar B. Helgason, Zhichao Ye, Yan Gao, Magnus Karlsson, Peter A. Andrekson, and Victor Torres-Company

Optica, vol. 11, no. 3, pp. 420-426, 2024.

Paper D

Chip-scale narrow-linewidth optical parametric oscillators

Yi Sun, Fuchuan Lei, Carlos E. Osornio-Martinez, Yan Gao, Dawson B. Bonneville, Meindert Dijkstra, Sonia M. García-Blanco, and Victor Torres-Company

submitted, 2026.